

## Effects of a subadiabatic layer on convection and dynamos in spherical wedge simulations

P.J. KÄPYLÄ<sup>a,b,c,d,e\*</sup>, M. VIVIANI<sup>d</sup>, M.J. KÄPYLÄ<sup>d,c</sup>, A. BRANDENBURG<sup>e,f,g,h</sup> and F. SPADA<sup>d</sup>

<sup>a</sup> Georg-August-Universität Göttingen, Institut für Astrophysik, Friedrich-Hund-Platz 1, D-37077 Göttingen, Germany

<sup>b</sup> Leibniz-Institut für Astrophysik, An der Sternwarte 16, D-14482 Potsdam, Germany

<sup>c</sup> ReSoLVE Centre of Excellence, Department of Computer Science, P.O. Box 15400, FI-00076 Aalto, Finland

<sup>d</sup> Max-Planck-Institut für Sonnensystemforschung, Justus-von-Liebig-Weg 3, D-37077 Göttingen, Germany

<sup>e</sup> NORDITA, KTH Royal Institute of Technology and Stockholm University, Roslagstullsbacken 23, SE-10691 Stockholm, Sweden

<sup>f</sup> Department of Astronomy, AlbaNova University Center, Stockholm University, SE-10691 Stockholm, Sweden

<sup>g</sup> JILA and Department of Astrophysical and Planetary Sciences, Box 440, University of Colorado, Boulder, CO 80303, USA

<sup>h</sup> Laboratory for Atmospheric and Space Physics, 3665 Discovery Drive, Boulder, CO 80303, USA

(January 3, 2019, Revision: 1.1)

We consider the effect of a subadiabatic layer at the base of the convection zone on convection itself and the associated large-scale dynamos in spherical wedge geometry. We use a heat conduction prescription based on the Kramers opacity law which allows the depth of the convection zone to dynamically adapt to changes in the physical characteristics such as rotation rate and magnetic fields. We find that the convective heat transport is strongly concentrated toward the equatorial and polar regions in the cases without a substantial radiative layer below the convection zone. The presence of a stable layer below the convection zone significantly reduces the anisotropy of radial enthalpy transport. Furthermore, the dynamo solutions are sensitive to subtle changes in the convection zone structure. We find that the kinetic helicity changes sign in the deeper parts of the convection zone at high latitudes in all runs. This region expands progressively toward the equator in runs with a thicker stably stratified layer.

**Keywords:** convection, turbulence, dynamos, magnetohydrodynamics

### 1. Introduction

Both differential rotation and dynamo action in late-type stars such as the Sun are driven by the interaction of turbulent convection and global rotation of the stars (e.g. [Miesch and Toomre 2009](#), [Brun and Browning 2017](#)). While a popular class of mean-field dynamos, known as the flux transport dynamos (e.g. [Dikpati and Charbonneau 1999](#)), rely on processes in the boundary layers at the base and near the surface of the convection zone (CZ), large-eddy simulations of stellar convection have demonstrated that solar-like magnetic activity can be obtained without the inclusion of such layers (e.g. [Ghizaru \*et al.\* 2010](#), [Käpylä \*et al.\* 2012](#), [Warnecke \*et al.\* 2014](#), [Passos and Charbonneau 2014](#), [Augustson \*et al.\* 2015](#), [Käpylä \*et al.\* 2016](#)). However, this does not necessarily imply that the solar dynamo works like the simu-

---

\*Corresponding author. Email: pkaepyl@uni-goettingen.de

lations suggest, because they face problems of their own. For example, numerical simulations appear to produce much higher velocity amplitudes at large horizontal scales in comparison to what is found with helioseismic inversions (Hanasoge *et al.* 2012, Gizon and Birch 2012).

There is another piece of evidence that also suggests that the velocities are too high in simulations. This evidence comes from simulations that adopt the solar luminosity and rotation rate: instead of a solar-like differential rotation profile with fast equator and slow poles, an anti-solar one with slow equator and fast poles is obtained. This is indicative of a lower rotational influence on the flow in simulations in comparison to the Sun (e.g. Gastine *et al.* 2014, Käpylä *et al.* 2014, Hotta *et al.* 2015). This discrepancy between observations and simulations is called the ‘convective conundrum’ (O’Mara *et al.* 2016). Furthermore, the simulated rotation profiles are nearly in Taylor-Proudman balance, corresponding to cylindrical isocontours of constant angular velocity (e.g. Brun and Toomre 2002, Miesch *et al.* 2006, Käpylä *et al.* 2011a) in comparison to more spoke-like isocontours inferred for the Sun (Schou *et al.* 1998).

A possible remedy to the Taylor-Proudman dilemma is to assume that the lower part of the CZ is slightly subadiabatic (Rempel 2005), in which case a thermal wind produced by the negative entropy fluctuations leads to a more conical angular velocity profile (Miesch *et al.* 2006). A related idea has been invoked to crack the convective conundrum: if convection is driven only in the near-surface layers by radiative cooling (Spruit 1997, Brandenburg 2016), the larger-scale convective modes such as giant cells are not excited, leading to a reduction of power at large horizontal scales (e.g. Cossette and Rast 2016). In this scenario the bulk of the revised CZ is being mixed due to overshooting by downflow plumes originating near the surface.

Recent numerical simulations indeed suggest that convection is driven by cooling near the surface (Cossette and Rast 2016, Käpylä *et al.* 2017b) and that the lower part of the convection zone is weakly subadiabatic (e.g. Tremblay *et al.* 2015, Käpylä *et al.* 2017b, Hotta 2017, Bekki *et al.* 2017, Karak *et al.* 2018, Nelson *et al.* 2018). Evidence of a changing structure of convection from a tree-like (decreasing number of downflow plumes with increasing depth) to a forest-like structure (constant number of plumes) has also been reported (Käpylä *et al.* 2017b). In the simulations of Hotta (2017), the extent of the subadiabatic region has been reported to encompass at most roughly 40 per cent of the combined depth of the convection and overshoot zones. In a subsequent study, Karak *et al.* (2018) found a similar effect in non-rotating hydrodynamic convection simulations at thermal Prandtl numbers above unity. However, the effect was significantly weaker in simulations including rotation. The main difference of the present study compared to that of Karak *et al.* (2018) is that we also include setups where overshoot and radiative layers are present, and investigate cases where dynamo action occurs.

Large-scale dynamos in stellar convective envelopes can also be affected by a subadiabatic layer at the base of the convection zone: such a layer can store magnetic flux (e.g. Browning *et al.* 2006) and it can possibly contribute to inverting the sign of kinetic helicity of the flow in the deep parts of the CZ (Duarte *et al.* 2016). Such inversion is a possible way out of the ‘modern dynamo dilemma’ that plagues current simulators: the equatorward migrating dynamo waves are most likely due to a region of negative radial shear within the CZ (Warnecke *et al.* 2014), which is not present in the Sun, except for the near-surface shear layer (NSSL); see Brandenburg (2005). The problem of the observed equatorward migration of the sunspot belts is a variation of Parker’s dynamo dilemma (Parker 1987) where the observed differential rotation profile and theoretically expected sign of kinetic helicity lead to poleward migration of activity belts (see also Deluca and Gilman 1986).

In the current study we present first results from convection-driven dynamo simulations in spherical wedges where stably stratified layers are present with a setup that is similar to that of the hydrodynamic Cartesian runs of Käpylä *et al.* (2017b), where a physics-based rather than a prescribed formulation for the heat conduction was used.

## 2. Model

Our simulation setup is similar to that used earlier (Käpylä *et al.* 2013, 2016, 2017a). However, the current models differ in a few key aspects from the previous studies. We solve the equations of fully compressible magnetohydrodynamics

$$\frac{\partial \mathbf{A}}{\partial t} = \mathbf{U} \times \mathbf{B} - \eta \mu_0 \mathbf{J}, \quad (1)$$

$$\frac{D \ln \rho}{Dt} = - \nabla \cdot \mathbf{U}, \quad (2)$$

$$\frac{D\mathbf{U}}{Dt} = \mathbf{g} - 2\boldsymbol{\Omega}_0 \times \mathbf{U} - \frac{1}{\rho}(\nabla p + \mathbf{J} \times \mathbf{B} + \nabla \cdot 2\nu \rho \mathbf{S}), \quad (3)$$

$$T \frac{Ds}{Dt} = \frac{1}{\rho} \left[ \eta \mu_0 \mathbf{J}^2 - \nabla \cdot (\mathbf{F}^{\text{rad}} + \mathbf{F}^{\text{SGS}}) - \Gamma_{\text{cool}} \right] + 2\nu \mathbf{S}^2, \quad (4)$$

where  $\mathbf{A}$  is the magnetic vector potential,  $\mathbf{U}$  is the velocity,  $\mathbf{B} = \nabla \times \mathbf{A}$  is the magnetic field,  $\eta$  is the magnetic diffusivity,  $\mu_0$  is the permeability of vacuum,  $\mathbf{J} = \nabla \times \mathbf{B} / \mu_0$  is the current density,  $D/Dt = \partial/\partial t + \mathbf{U} \cdot \nabla$  is the advective time derivative,  $\rho$  is the density,  $\mathbf{g} = -GM_\odot \hat{\mathbf{r}}/r^2$  is the acceleration due to gravity, where  $G = 6.67 \cdot 10^{-11} \text{ N m}^2 \text{ kg}^{-2}$  is the universal gravitational constant, and  $M_\odot = 2.0 \cdot 10^{30} \text{ kg}$  is the solar mass,  $\boldsymbol{\Omega}_0 = (\cos \theta, -\sin \theta, 0)\Omega_0$  is the angular velocity vector, where  $\Omega_0$  is the rotation rate of the frame of reference,  $\nu$  is the kinematic viscosity,  $p$  is the pressure, and  $s$  is the specific entropy with  $Ds = c_V D \ln p - c_P D \ln \rho$ , where  $c_V$  and  $c_P$  are the specific heats in constant volume and pressure, respectively. The gas is assumed to obey the ideal gas law,  $p = \mathcal{R} \rho T$ , where  $\mathcal{R} = c_P - c_V$  is the gas constant. The rate of strain tensor is given by

$$S_{ij} = \frac{1}{2}(U_{i;j} + U_{j;i}) - \frac{1}{3}\delta_{ij} \nabla \cdot \mathbf{U}, \quad (5)$$

where the semicolons refer to covariant derivatives (Mitra *et al.* 2009). The radiative flux is given by

$$\mathbf{F}^{\text{rad}} = -K \nabla T, \quad (6)$$

where  $K$  is the heat conductivity, which is allowed to vary in a dynamic and local fashion. We use two heat conduction schemes, where  $K$  is either a fixed function of height  $K = K(r)$  or it depends on density and temperature  $K = K(\rho, T)$ . In the former case we use the same profile as defined in Käpylä *et al.* (2013). In the latter case  $K$  is computed from

$$K = \frac{16\sigma_{\text{SB}} T^3}{3\kappa\rho}, \quad (7)$$

where  $\sigma_{\text{SB}}$  is the Stefan-Boltzmann constant and  $\kappa$  is the opacity. The latter is assumed to obey a power law

$$\kappa = \kappa_0 (\rho/\rho_0)^a (T/T_0)^b, \quad (8)$$

where  $\rho_0$  and  $T_0$  are reference values of density and temperature. Combining (7) and (8) gives (Barekat and Brandenburg 2014)

$$K(\rho, T) = K_0 (\rho/\rho_0)^{-(a+1)} (T/T_0)^{3-b}. \quad (9)$$

In the current study we use the combination  $a = 1$  and  $b = -7/2$ , which corresponds to the Kramers opacity law for free-free and bound-free transitions (Weiss *et al.* 2004). This scheme has been used both in Cartesian (Brandenburg *et al.* 2000, Käpylä *et al.* 2017b) and in spherical wedge (Käpylä *et al.* 2018a) simulations of convection.

The subgrid scale (SGS) flux is given by

$$\mathbf{F}^{\text{SGS}} = -\chi_{\text{SGS}}\rho T \nabla s', \quad (10)$$

where  $\chi_{\text{SGS}}$  is the (constant) SGS diffusion coefficient for the entropy fluctuation  $s'(r, \theta, \phi) = s - \langle s \rangle_{\theta\phi}$ , where  $\langle s \rangle_{\theta\phi}$  is the horizontally averaged or spherically symmetric part of the specific entropy.

The last term on the right-hand side of (4) models the cooling near the surface of the star:

$$\Gamma_{\text{cool}} = -\Gamma_0 f(r) (T_{\text{cool}} - \langle T \rangle_{\theta\phi}), \quad (11)$$

where  $\Gamma_0$  is a cooling luminosity,  $\langle T \rangle_{\theta\phi}$  is the horizontally averaged temperature, and  $T_{\text{cool}} = T_{\text{cool}}(r)$  is a radius-dependent cooling temperature coinciding with the initial isentropic stratification. In our previous studies (Käpylä *et al.* 2010, 2011b), we cooled the near-surface layers toward an isothermal state. The main effect of the changed cooling profile is that no strongly subadiabatic isothermal layer forms near the surface.

The simulations were performed using the PENCIL CODE<sup>1</sup>. The code employs a high-order finite difference method for solving the compressible equations of MHD.

### 2.1. System parameters and diagnostics quantities

The wedges used in the current simulations span  $r_{\text{in}} < r < R_{\odot}$  in radius, where  $r_{\text{in}} = 0.7R_{\odot}$  and  $R_{\odot} = 7 \cdot 10^8$  m is the solar radius,  $\theta_0 < \theta < 180^\circ - \theta_0$  in colatitude, where  $\theta_0 = 15^\circ$ , and  $0 < \phi < 90^\circ$  in longitude. Our simulations are defined by the energy flux imposed at the bottom boundary,  $F_b = -(K\partial T/\partial r)|_{r=r_{\text{in}}}$ , the values of  $K_0$ ,  $a$ ,  $b$ ,  $\rho_0$ ,  $T_0$ ,  $\Omega_0$ ,  $\nu$ ,  $\eta$ ,  $\chi_{\text{SGS}}$ , and the fixed profile of  $K$  in cases where the Kramers opacity law is not used. Furthermore, the radial profile of  $f(r)$  is piecewise constant with  $f(r) = 0$  in  $r_{\text{in}} < r < 0.98R_{\odot}$ , and smoothly connecting to  $f(r) = 1$  above  $r = 0.98R_{\odot}$ . We use a significantly higher luminosity and thus a higher Mach number than what is estimated for the Sun to avoid the time step being too severely limited by sound waves. This also necessitates a correspondingly higher rotation rate to capture the same rotational influence on the flow in the simulations in comparison to the Sun; see appendix A of Käpylä *et al.* (2018a) for a thorough description of this procedure. This study also indicates that the results depend only weakly on the Mach number. The ratio  $L_{\text{ratio}} = L_0/L_{\odot}$ , where  $L_0$  is the luminosity in the simulations and  $L_{\odot} = 3.83 \cdot 10^{26}$  W is the corresponding solar value, quantifies the luminosity. The non-dimensional luminosity is given by

$$\mathcal{L} = \frac{L_0}{\rho_0 (GM_{\odot})^{3/2} R_{\odot}^{1/2}}. \quad (12)$$

The initial stratification is determined by the non-dimensional pressure scale height at the surface

$$\xi_0 = \frac{\mathcal{R}T_1}{GM_{\odot}/R_{\odot}}, \quad (13)$$

where  $T_1$  is the temperature at the surface ( $r = R_{\odot}$ ).

The relations between viscosity, magnetic diffusivity, and SGS diffusion are given by the Prandtl numbers

$$\text{Pr}_{\text{SGS}} = \nu/\chi_{\text{SGS}}, \quad \text{Pm} = \nu/\eta. \quad (14)$$

<sup>1</sup><https://github.com/pencil-code/>

We use  $\text{Pr}_{\text{SGS}} = \text{Pm} = 1$  in all of our runs. The Prandtl number is related to the radiative conductivity,

$$\text{Pr} = \nu/\chi, \quad (15)$$

where  $\chi = K/c_{\text{P}}\rho$  is the radiative diffusivity, which varies as a function of radius, latitude, and time. The efficiency of convection is quantified by the Rayleigh number

$$\text{Ra} = \frac{GM_{\odot}(\Delta r)^4}{\nu\chi_{\text{SGS}}R_{\odot}^2} \left( -\frac{1}{c_{\text{P}}} \frac{ds_{\text{hs}}}{dr} \right)_{r_{\text{m}}}, \quad (16)$$

where  $\Delta r = 0.3R_{\odot}$  is the depth of the layer,  $s_{\text{hs}}$  is the entropy in a one-dimensional non-convecting hydrostatic model, evaluated at the middle of the domain at  $r_{\text{m}} = 0.85R_{\odot}$ . We note that in the cases with a Kramers-based heat conduction prescription, only a very thin surface layer is convectively unstable (see, e.g., Figure 7 of [Brandenburg 2016](#)), such that  $\text{Ra} < 0$  at  $r = r_{\text{m}}$ . We additionally quote the Nusselt number, which describes the efficiency of convection in comparison to radiative diffusion (e.g. [Hurlburt et al. 1984](#), [Brandenburg 2016](#)):

$$\text{Nu} = \nabla_{\text{rad}}/\nabla_{\text{ad}}, \quad (17)$$

just below the cooling layer at  $r = 0.98R_{\odot}$ , where

$$\nabla_{\text{rad}} = \frac{\mathcal{R}}{Kg} F_{\text{tot}} \quad \text{and} \quad \nabla_{\text{ad}} = 1 - \frac{1}{\gamma}, \quad (18)$$

are the radiative and adiabatic temperature gradients,  $g = |\mathbf{g}|$ ,  $F_{\text{tot}} = L_0/(4\pi r^2)$ , and  $\gamma = c_{\text{P}}/c_{\text{V}}$ . For runs with a fixed  $K$ ,  $\text{Nu}$  remains constant throughout the duration of the simulation whereas in the cases with Kramers conductivity the saturated value,  $\text{Nu}_{\text{sat}}$  differs from the initial value  $\text{Nu}$ . The effect of rotation is controlled by the Taylor number

$$\text{Ta} = (2\Omega_0\Delta r^2/\nu^2)^2. \quad (19)$$

The fluid and magnetic Reynolds numbers are

$$\text{Re} = \frac{u_{\text{rms}}}{\nu k_1} \quad \text{and} \quad \text{Re}_{\text{M}} = \frac{u_{\text{rms}}}{\eta k_1}, \quad (20)$$

respectively, where  $u_{\text{rms}} = \sqrt{\frac{3}{2}(U_r^2 + U_{\theta}^2)}$  is the volume averaged rms velocity and  $U_{\phi}^2$  has been replaced by  $(U_r^2 + U_{\theta}^2)/2$  to avoid contributions from differential rotation (cf. [Käpylä et al. 2011b](#)). The inverse of the basic wavenumber  $k_1 = 2\pi/\Delta r \approx 21/R_{\odot}$  is used to characterise the radial extent of convection cells.

The rotational influence on the flow is quantified by the Coriolis number

$$\text{Co} = \frac{2\Omega_0}{u_{\text{rms}}k_1}. \quad (21)$$

Mean quantities refer either to azimuthal (denoted by an overbar) or horizontal averages (denoted by angle brackets with subscript  $\theta\phi$ ). Additional time averaging is also performed unless stated otherwise.

## 2.2. Initial and boundary conditions

The initial stratification is polytropic with index  $n = 1.5$  corresponding to an isentropic stratification. We use  $\xi_0 = 0.01$ , which results in an initial density contrast of roughly 77. In cases with a fixed heat conductivity profile, the value of  $K$  at  $r = r_{\text{in}}$  is set such that the flux through the lower boundary is  $L_0/4\pi r_{\text{in}}^2$ . The luminosity  $L_0$  is based on the total horizontal area of the star, although the simulations cover only a fraction of the full  $4\pi$  area. The flux

Table 1. Summary of the runs. All runs have  $L_{\text{ratio}} = 2.1 \cdot 10^5$ ,  $\Omega_0 = 3\Omega_{\odot}$ ,  $\text{Pr}_{\text{SGS}} = \text{Pr}_{\text{M}} = 1$ ,  $\nu = 1.46 \cdot 10^8 \text{ m}^2 \text{ s}^{-1}$ ,  $\text{Ta} = 2.33 \cdot 10^7$ ,  $\xi_0 = 0.01$ , and grid resolution  $144 \times 288 \times 144$ .

Run	Ra [ $10^7$ ]	Nu	Nu <sub>sat</sub>	Re	Co	$r_{\text{BZ}}$	$r_{\text{DZ}}$	$r_{\text{OZ}}$	$d_{\text{BZ}}$	$d_{\text{DZ}}$	$d_{\text{OZ}}$	$\Delta t$ [yr]	$K$	$\tilde{K}_0$
HDp	3.0	156	156	36 (36)	–	(0.76	0.70	0.70	0.24	0.06	0.00)	35	profile	–
HD1	–	3167	2599	34 (33)	–	(0.76	0.71	0.70	0.24	0.06	0.01)	10	Kramers	1.0
HD2	–	1843	1524	31 (29)	–	(0.79	0.73	0.70	0.21	0.07	0.03)	10	Kramers	1.7
HD3	–	972	786	28 (25)	–	0.82	0.77	0.71	0.18	0.06	0.06	12	Kramers	3.2
HD4	–	590	440	26 (22)	–	0.85	0.80	0.73	0.15	0.05	0.07	11	Kramers	5.4
RHDp	3.0	156	156	27 (27)	4.6 (4.6)	(0.75	0.70	0.70	0.25	0.05	0.00)	49	profile	–
RHD1	–	3167	3034	30 (30)	4.1 (4.1)	(0.75	0.70	0.70	0.25	0.05	0.00)	29	Kramers	1.0
RHD2	–	1843	1772	28 (26)	4.3 (3.5)	(0.78	0.74	0.71	0.22	0.04	0.03)	27	Kramers	1.7
RHD3	–	972	882	25 (22)	4.8 (3.0)	0.79	0.78	0.72	0.21	0.01	0.06	29	Kramers	3.2
RHD4	–	590	479	23 (19)	5.3 (2.5)	0.82	0.81	0.76	0.18	0.01	0.05	22	Kramers	5.4
MHDp	3.0	156	156	27 (27)	4.5 (4.5)	(0.76	0.70	0.70	0.24	0.06	0.00)	44	profile	–
MHD1	–	3167	3004	30 (30)	4.1 (4.1)	(0.76	0.70	0.70	0.24	0.06	0.00)	63	Kramers	1.0
MHD2	–	1843	1743	27 (25)	4.5 (3.6)	(0.78	0.74	0.71	0.22	0.05	0.03)	74	Kramers	1.7
MHD3	–	972	868	23 (20)	5.3 (3.2)	0.80	0.78	0.72	0.20	0.02	0.06	64	Kramers	3.2
MHD4	–	590	473	21 (18)	5.8 (2.7)	0.82	0.81	0.77	0.18	0.01	0.04	72	Kramers	5.4

The values of  $r_{\text{BZ}}$ ,  $r_{\text{DZ}}$ ,  $r_{\text{OZ}}$ ,  $d_{\text{BZ}}$ ,  $d_{\text{DZ}}$ , and  $d_{\text{OZ}}$  for Runs RHDp, RHD1, RHD2, MHDp, MHD1, and MHD2, where strong latitudinal variations are seen, are listed in parentheses to indicate uncertainty. The value of Nu refers to the initial state and Nu<sub>sat</sub> to the saturated convective state, both computed from (17). The values in brackets for Re and Co are calculated taking the volume averaged  $u_{\text{rms}}$  from the revised convection zone ( $r_{\text{DZ}} < r < R_{\odot}$ ) using  $k_1 = 2\pi/(R_{\odot} - r_{\text{DZ}})$  as the wavenumber.

at the outer radius, however, is initially much lower and the convective instability arises from the fact that the system is not in thermodynamic equilibrium driven by the efficient surface cooling (see e.g. Käpylä *et al.* 2013). In the cases with Kramers heat conductivity, the value of  $K$  at the bottom of the domain is varied by changing the value of  $\tilde{K}_0$  in (9) to probe the influence it has on the depth of the convection zone. In the fiducial case, a nominal value  $\tilde{K}_0^{\text{nom}}$  is chosen such that  $F_{\text{rad}} = F_{\text{tot}}$  at the bottom of the domain. We probe a set of runs where the value of  $\tilde{K}_0 = K_0/\tilde{K}_0^{\text{nom}}$  is increased. These runs correspond to more efficient radiative diffusion for a given thermal stratification. The expectation is that an increasing value of  $\tilde{K}_0$  leads to the formation of a stably stratified radiative layer at the bottom of the domain.

The radial and latitudinal boundaries are assumed impenetrable and stress-free for the flow. On the bottom boundary, a fixed heat flux is prescribed and the temperature is fixed on the outer boundary. On the latitudinal boundaries, the gradients of thermodynamic quantities are set to zero; see Käpylä *et al.* (2013). For the magnetic field we apply a vertical field condition at the upper, and a perfect conductor condition at the lower boundary. On the latitudinal boundaries the field is assumed to be tangential to the boundary. These conditions are given by:

$$\frac{\partial A_r}{\partial r} = 0, \quad \frac{\partial^2 A_{\theta}}{\partial r^2} = -\frac{2}{r} \frac{\partial A_{\theta}}{\partial r}, \quad \frac{\partial^2 A_{\phi}}{\partial r^2} = -\frac{2}{r} \frac{\partial A_{\phi}}{\partial r} \quad (r = r_{\text{in}}), \quad (22)$$

$$A_r = 0, \quad \frac{\partial A_{\theta}}{\partial r} = -\frac{A_{\theta}}{r}, \quad \frac{\partial A_{\phi}}{\partial r} = -\frac{A_{\phi}}{r} \quad (r = R_{\odot}), \quad (23)$$

$$A_r = \frac{\partial A_{\theta}}{\partial \theta} = A_{\phi} = 0. \quad (\theta = \theta_0, \pi - \theta_0). \quad (24)$$

Equation (22) differs from previously used conditions (see, e.g., equation (10) of Käpylä *et al.* 2013), where instead the tangential electric field was assumed to vanish on the boundary. We show in Käpylä *et al.* (2018a) that the differences between the current boundary conditions and those used in Käpylä *et al.* (2013) are minor. The azimuthal direction is periodic for all quantities. The velocity and magnetic fields are initialised with random Gaussian noise fluctuations with amplitudes on the order of 0.1 m s<sup>-1</sup> and 0.1 Gauss, respectively.

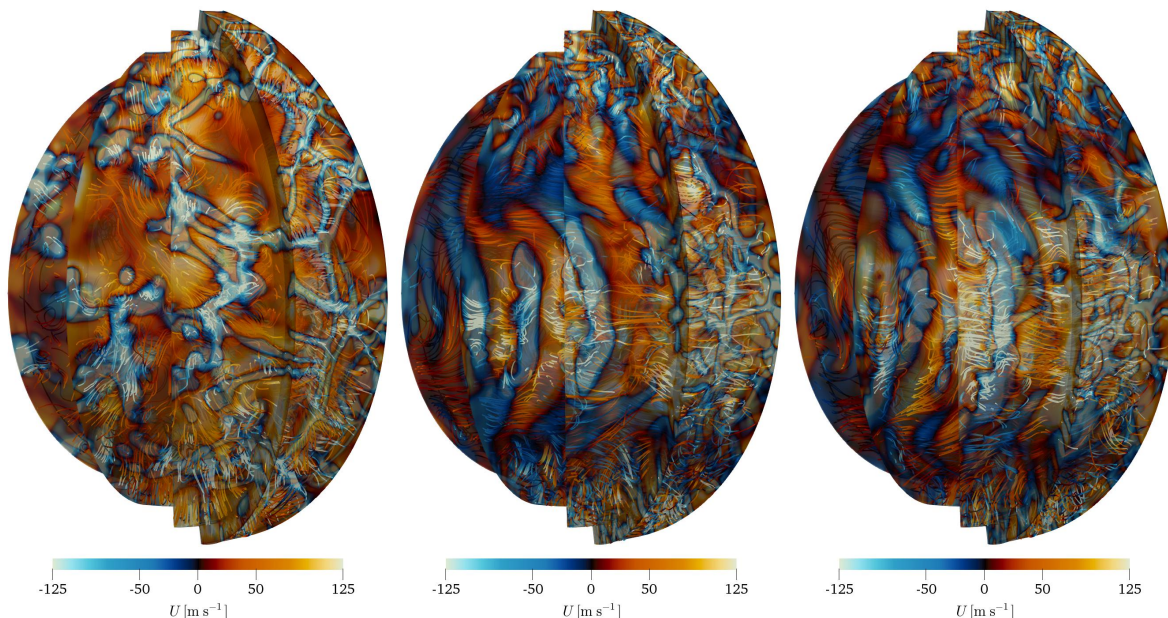


Figure 1. Streamlines of the total velocity and contours of vertical velocity at the periphery in snapshots of Runs HD2 (left), RHD2 (middle), and MHD2 (right). The colour-coding of both is indicated at the bottom of each panel. The horizontal cuts from left to right are shown from depths  $r/R_{\odot} = 0.78, 0.85, 0.92,$  and  $0.99$ . Animated visualisations of Runs HD2 and RHD2 are available in the online material (colour online).

### 3. Results

We perform three sets of simulations denoted as HD, RHD, and MHD. In Set HD, we model non-rotating convection, where  $\tilde{K}_0$  is varied to control the depth of the convection zone. The effect of increasing  $\tilde{K}_0$  is to make radiative diffusion more efficient. This is particularly important in the deep parts of the domain where the temperature is high due to the strong temperature dependency of the heat conduction ( $K \propto T^{6.5}$ , see (9)). Thus the expectation is that with higher values of  $\tilde{K}_0$ , a radiative layer develops at the bottom of the domain. In the RHD runs, we take the HD runs and add rotation with  $\Omega_0 = 3\Omega_{\odot}$ , where  $\Omega_{\odot} = 2.7 \cdot 10^{-6} \text{ s}^{-1}$  is the mean solar rotation rate. In the MHD set, magnetic fields are added to the RHD setup to study the effects of stably stratified layers on the dynamo. Each set consists of four runs, denoted by a suffix running from 1 to 4, where the value of  $K_0$  is systematically increased. A run with a fixed profile of  $K$ , denoted by a suffix ‘p’, is used as a reference in each set with the same variation of physical ingredients. The runs are listed in table 1.

The value of  $\Omega_0$  in the rotating simulations is chosen such that a solar-like differential rotation is obtained. The current setups with a Kramers-based heat conduction still tend to produce anti-solar differential rotation at solar luminosity and rotation rate. Visualisations of the flow fields realized in representative hydrodynamic runs without (HD2) and with rotation (RHD2), and a corresponding MHD run (MHD2) are shown in figure 1. The non-rotating cases qualitatively resemble mixing length ideas in that the horizontal scale of the convective eddies increases as a function of depth. The rotating cases are dominated by banana cells (e.g. Busse 1970, Gilman and Miller 1986) in the equatorial regions and by small scale convection at high latitudes, and this carries over also to the magnetic cases. The flow structure in the current MHD runs is typically very similar to the corresponding RHD runs. The convective scales show significantly less variation in depth in comparison to non-rotating convection.

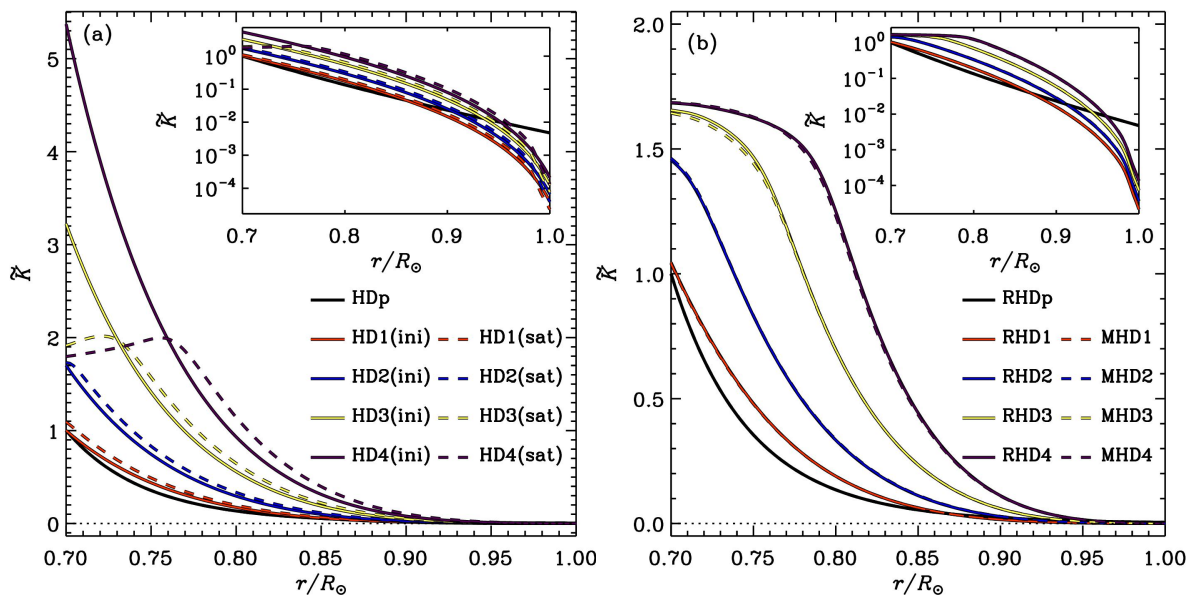


Figure 2. (a) Profiles of the initial (solid lines) and saturated (dashed) mean heat conductivity profiles  $\tilde{K} = \langle K \rangle_{\theta\phi} / K_0^{\text{nom}}$ . (b) Same as (a) but for sets RHD (solid lines) and MHD (dashed lines) from the saturated states (colour online).

### 3.1. Convective energy transport and structure of the convection zone

In an earlier study, Käpylä *et al.* (2017b) found that a stably stratified layer, where the enthalpy flux is nevertheless directed outward, develops at the bottom of the convection zone if a smoothly varying profile for the heat conduction is used. Furthermore, when the Kramers opacity law is applied, the depth of the convection zone is a result of the simulation rather than a priori fixed. Here we extend these studies to more realistic spherical geometry and take into account global rotation and dynamo-generated magnetic fields.

We begin by inspecting horizontally averaged diagnostic quantities from our simulations. The profiles of  $\langle K \rangle_{\theta\phi}$  from the HD set in the initial and thermally saturated states are shown in figure 2(a). The mean  $K$ -profiles in Runs HD1 and HD2 remain almost unaffected in the thermally relaxed regime. In Runs HD3 and HD4, the lower parts of the domain ( $r \lesssim 0.73R_\odot$  and  $r \lesssim 0.76R_\odot$ , respectively), where  $\langle K \rangle_{\theta\phi}$  is the largest, become convectively stable and a lower temperature gradient is sufficient to carry the luminosity through these layers. In the RHD and MHD runs the temperature gradient is steeper throughout and the values of  $\langle K \rangle_{\theta\phi}$  are reduced overall; see figure 2(b). Furthermore, the MHD runs differ only marginally from their RHD counterparts. This suggests a relatively weak influence of magnetic fields in the current simulations. However, we note that the magnetic Reynolds number in the current simulations is relatively moderate and clearly below the excitation threshold for small-scale dynamo action.

The horizontally and temporally averaged superadiabatic temperature gradient  $\nabla - \nabla_{\text{ad}}$  is shown for all of our runs in figure 3(a)–(b). We find that in Runs HDp and HD1, as well as their rotating and MHD counterparts,  $\nabla - \nabla_{\text{ad}}$  is close to zero in the bulk of the domain, with a mildly subadiabatic layer near the base. Furthermore, with increasing  $K_0$ , a gradually deeper subadiabatic layer forms in the lowermost parts of the domain. The values of  $\nabla - \nabla_{\text{ad}}$  in the ‘3’ and ‘4’ runs of all sets are on the order of  $-0.19 \dots -0.16$ . This is close to that of the hydrostatic case which approaches a polytropic state with index  $n = 3.25$  (Barekat and Brandenburg 2014). Panel (c) of figure 3 shows the superadiabatic temperature gradient from a standard solar model produced with the Yale Rotating Stellar Evolution Code (YREC) (Demarque *et al.* 2008, Spada *et al.* 2017). The minimum values of  $\nabla - \nabla_{\text{ad}}$  in the radiative

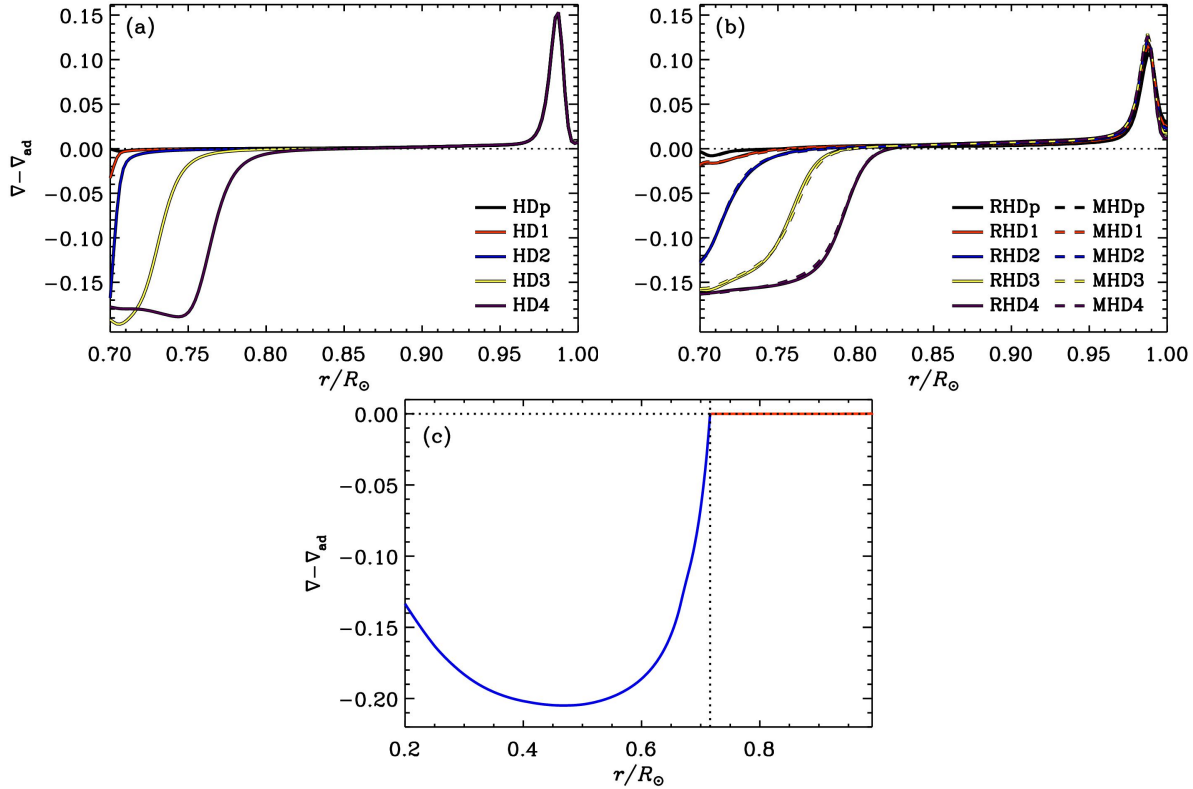


Figure 3. (a) Profiles of the superadiabatic temperature gradient  $\nabla - \nabla_{\text{ad}}$  from non-rotating HD runs. (b) Same as (a) but for sets RHD (solid lines) and MHD (dashed). Panel (c) shows  $\nabla - \nabla_{\text{ad}}$  from a standard solar model in the range  $r/R_{\odot} = 0.2 \dots 0.99$ . The blue (red) curve corresponds to the radiative (convection) zone with the interface marked by the dotted vertical line at  $r/R_{\odot} = 0.716$  (colour online).

layer in this model and our simulations are comparable and about  $-0.2$ .

The enthalpy flux is defined as

$$\overline{F}_i^{\text{enth}} = c_P \overline{(\rho u_i)' T'}, \quad (25)$$

where the primes denote fluctuation from the azimuthal mean denoted by an overbar. We use the same nomenclature as in Käpylä *et al.* (2017b) to distinguish the different layers in the domain (see also Brandenburg *et al.* 2000, Tremblay *et al.* 2015). This entails classifying the layers by the signs of the radial enthalpy flux  $\overline{F}_r^{\text{enth}}$  and the radial gradient of entropy,  $\nabla_r \bar{s} = \partial \bar{s} / \partial r$ , see table 2. The bottom of the buoyancy zone (BZ) is where  $\nabla_r \bar{s}$  changes from negative to positive, whereas the bottom of the Deardorff zone (DZ) is where  $\overline{F}_r^{\text{enth}}$  changes from positive to negative; see Brandenburg (2016) for an explanation of a non-gradient contribution to  $\overline{F}_r^{\text{enth}}$  by Deardorff (1966). Finally, the bottom of the overshoot zone (OZ) is where the  $|\overline{F}_r^{\text{enth}}|$  falls below a threshold value, here chosen to be 2.5 per cent of the total flux corresponding to luminosity  $L_0$ . In the commonly accepted view, the convection zone consists of the Schwarzschild-unstable layer without Deardorff zone (e.g. Zahn 1991). This coincides with the predictions from standard mixing length theory (e.g. Vitense 1953). In our revised view, the convection zone (CZ) is considered to encompass both the BZ and the DZ.

We show the time-averaged luminosity of the radial enthalpy flux,  $L_r^{\text{enth}} = 4\pi r^2 \overline{F}_r^{\text{enth}}$  and the direction of vectorial enthalpy flux,  $\overline{\mathbf{F}}^{\text{enth}} = (\overline{F}_r^{\text{enth}}, \overline{F}_\theta^{\text{enth}}, 0)$  in the meridional plane for a selection of runs in figure 4. In the non-rotating, hydrodynamic run HD1, the enthalpy flux is directed radially outward and approximately uniformly distributed in latitude with the exception of regions in the immediate vicinity of the latitudinal boundaries where the enthalpy

Table 2. Classification of zones.

Quantity/zone	Buoyancy (BZ)	Deardorff (DZ)	Overshoot (OZ)	Radiation (RZ)
$\overline{F}_r^{\text{enth}}$	$> 0$	$> 0$	$< 0$	$\approx 0$
$\nabla_r \bar{s}$	$< 0$	$> 0$	$> 0$	$> 0$

flux is enhanced. The differences between Runs HDp and HD1 are very minor in that both develop a DZ, covering roughly 20 per cent of the depth of the domain, at the base of the CZ. No appreciable overshoot region develops in either run. This is unsurprising because the heat conductivity in these models is chosen such that it just delivers the input flux through the lower boundary and decreases rapidly in the upper layers, necessitating convection to transport some fraction of the energy there. Increasing the value of  $\tilde{K}_0$  (from Runs HD2 to HD4) enhances the radiative diffusion—in particular in the deep parts where the temperature is high. This leads gradually to the formation of a radiative zone (RZ) at the base of the domain; see figure 4(c). In the non-rotating case it is meaningful to average over latitude and to obtain estimates of the depths of the different layers. These are listed as  $d_{\text{BZ}}$ ,  $d_{\text{DZ}}$ , and  $d_{\text{OZ}}$  in table 1. We note that only in Runs HD3 and HD4 the domain is deep enough to allow the formation of an RZ and that the depths of the DZ and/or OZ are thus underestimated for Runs HDp, HD1, and HD2. A similar argument applies to the runs presented by Bekki *et al.* (2017) and Karak *et al.* (2018). In Runs HD3 and HD4, the subadiabatic but mixed layers (DZ and OZ) cover 38 and 44 per cent of the total depth of the mixed zone. This is in good agreement with the results from local simulations (e.g. Käpylä *et al.* 2017b, Hotta 2017).

This picture is radically altered in the rotating cases; see the middle and lower panels of figure 4. The most prominent new feature is the strong latitude dependence of the radial enthalpy flux: the energy transport is strongly concentrated toward high latitudes and near the equator. Comparing figures 4(d)–(f) and 4(g)–(i) shows that the qualitative differences between the RHD and MHD runs are small. This is also the case for most other diagnostics and thus we will mostly discuss the MHD cases in what follows. A major difference between Runs MHDp and MHD1 is that in the former, the enthalpy flux is roughly equally efficient at high and low latitudes ( $\Theta \gtrsim 55^\circ$  and  $\Theta \lesssim 30^\circ$ , where  $\Theta = 90^\circ - \theta$  is the latitude), whereas in the latter the high latitude flux is suppressed. Another difference is that in Run MHDp the Deardorff layer at mid-latitudes ( $20^\circ \lesssim \Theta \lesssim 35^\circ$ ) covers almost the entire depth of the domain whereas in Run MHD1 the latitude variation is less extreme although still substantial; see the solid black and white lines in figure 4(g) and (h). Near the equator ( $\Theta \lesssim 10^\circ$ ), the Deardorff layer is either very thin (MHDp) or missing completely (MHD1). A possible explanation to the very deep mid-latitude Deardorff layer in Run MHDp is that the current simulations are only moderately supercritical in terms of the Rayleigh number and that convection is dominated by polar and equatorial modes in such parameter regimes (e.g. Gilman 1977). This is exacerbated by the rigid combination of a fixed heat conductivity profile and a constant temperature boundary condition applied at the radial top boundary. The reason why the Deardorff zone is significantly shallower in Run MHD1 is because, unlike in Run MHDp with a fixed  $K$ -profile, the heat conductivity adapts in response to changes in the thermal structure. Convectively stable mid-latitudes have been reported from similar simulation setups with fixed  $K$ -profile and surface temperature by Käpylä *et al.* (2011b). However, in cases where, for example, a black body radiation condition is applied at the surface, the mid-latitudes remain convectively unstable and allow for significant latitudinal variation of the surface temperature (Warnecke *et al.* 2016, Käpylä *et al.* 2018a). This is likely due to the enhanced luminosity used in the current simulations. We also note that in the rotating cases the heat flux is mostly radial near the equator, but more inclined with the rotation vector at high latitudes. This is a manifestation of latitudinal turbulent heat flux, which is often invoked to break the Taylor-

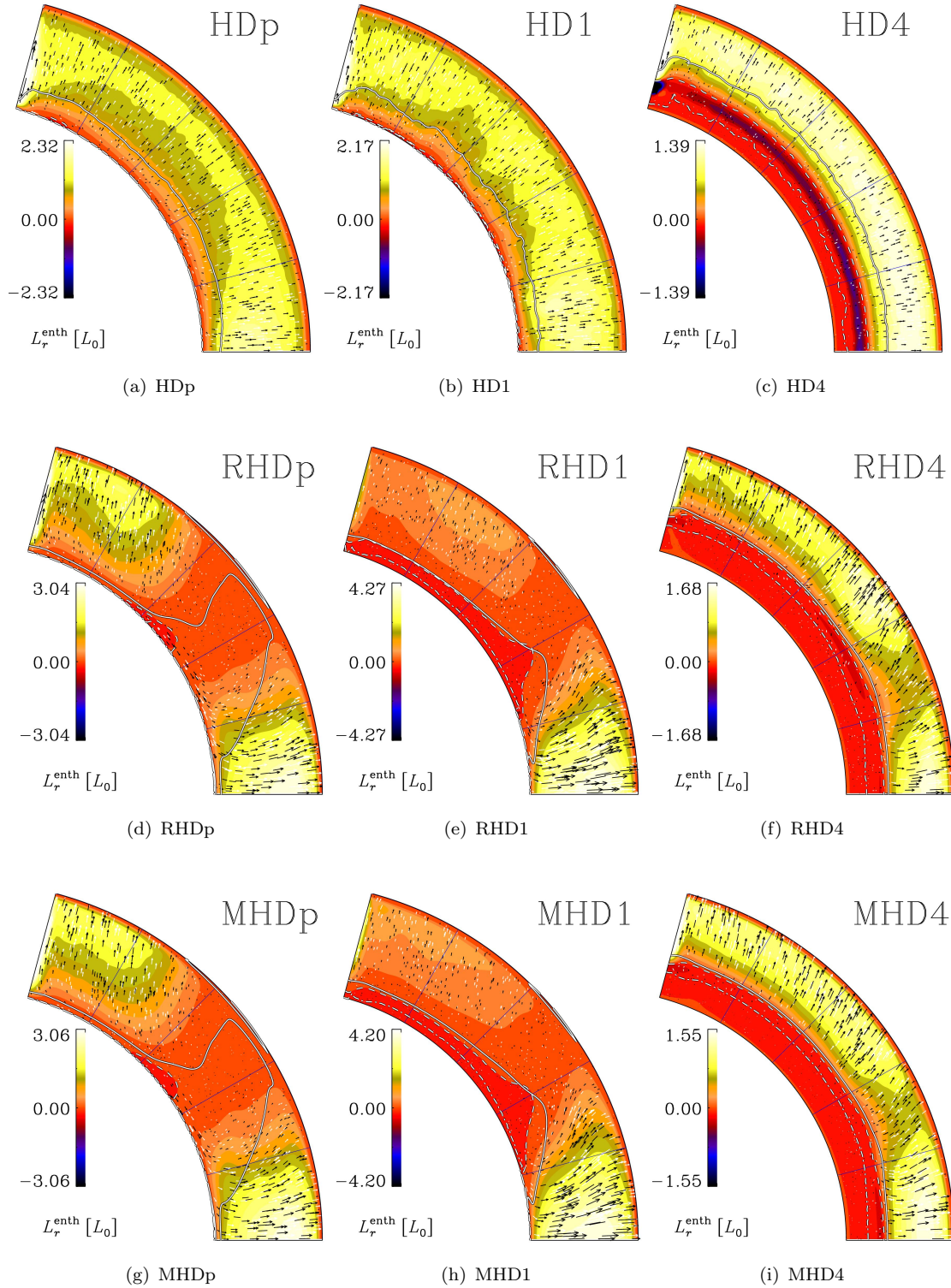


Figure 4. Colour contours: time-averaged luminosity of the radial enthalpy flux normalised by the total luminosity from non-rotating, hydrodynamic runs HDp, HD1, and HD4 (top row), rotating runs RHDp, RHD1, and RHD4 (middle row), and dynamo runs MHDp, MHD1, and MHD4 (lower row). The arrows indicate the magnitude and direction of the vectorial enthalpy flux,  $\overline{\mathbf{F}}^{\text{enth}} = (\overline{F}_r^{\text{enth}}, \overline{F}_\theta^{\text{enth}}, 0)$  in the meridional plane. The black and white solid, dashed, and dash-dotted lines indicate the bottoms of the buoyancy, Deardorff, and overshoot zones, respectively. The thin blue lines indicate latitudes  $15^\circ$ ,  $30^\circ$ ,  $45^\circ$ , and  $60^\circ$  (colour online).

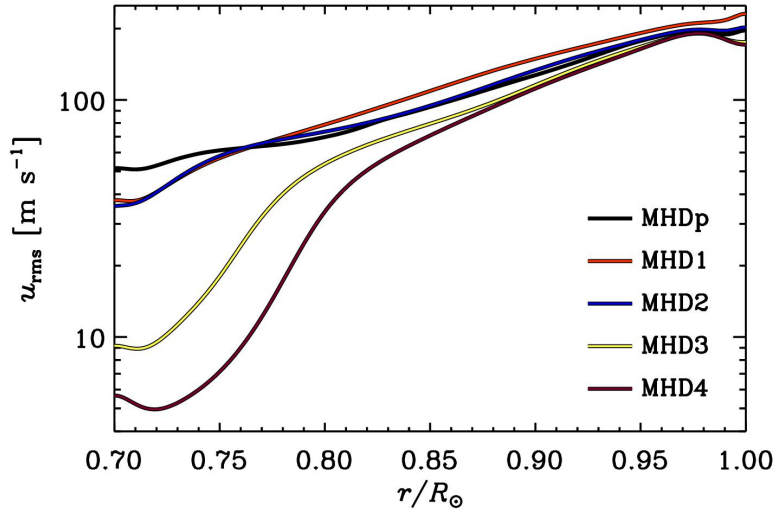


Figure 5. Horizontally averaged rms velocity  $u_{\text{rms}}$  from the runs in the MHD set (colour online).

Proudman balance in the Sun (e.g. [Brandenburg \*et al.\* 1992](#), [Kitchatinov and Rüdiger 1995](#)). A poleward enthalpy flux has been reported in numerous earlier studies (e.g. [Pulkkinen \*et al.\* 1993](#), [Rüdiger \*et al.\* 2005](#), [Käpylä \*et al.\* 2011b](#), [Brun \*et al.\* 2017](#)).

The strong latitudinal variation of the depths of the various layers render latitudinal averaging of  $r_{\text{BZ}}$ ,  $r_{\text{DZ}}$ , and  $r_{\text{OZ}}$  useless in these cases. In runs where an RZ develops (‘3’ and ‘4’ runs in each set), the latitudinal variation of the depths of the different zones and of the enthalpy flux are significantly weaker, see figure 4(f) and (i). However, for completeness, we list the latitudinally averaged coordinates of the bottoms of BZ, DZ, and OZ and the depths of the corresponding layers for all runs in table 1. The values for runs RHDp, RHD1, RHD2, MHDp, MHD1, and MHD2, where strong latitudinal variations are seen, are listed in parentheses and should be considered as uncertain. We found that the DZ diminishes substantially in Runs MHD3 and MHD4 in comparison to the non-rotating case HD3 and HD4, whereas the depth of the OZ is influenced less. It is also noteworthy that in the rotating Kramers-based Runs RHD1 and MHD1, the overall velocities, measured by the Reynolds numbers, are higher than in the fixed profile runs RHDp and MHDp; see the fifth column of table 1.

Figure 5 shows the temporally and horizontally averaged rms velocity from the runs in the MHD set with the same definition of  $u_{\text{rms}}$  as used in (20). The velocities near the surface are not much affected by the appearance of a radiative layer in the deep parts. A significant decrease of  $u_{\text{rms}}$  in the latter occurs only for the ‘3’ and ‘4’ runs in each set of simulations. In such cases the definitions of the Reynolds and Coriolis numbers in equations (20) and (21), respectively, become inaccurate. We thus provide these diagnostics computed using the rms velocity and the depth of the revised convection zone  $r_{\text{DZ}} < r < R_{\odot}$  in brackets in the fifth and sixth columns of table 1.

Our earlier Cartesian study indicated that the downflows are mostly responsible for the enthalpy flux in non-rotating overshooting convection (cf. Figure 2(c) of [Käpylä \*et al.\* 2017b](#)). However, convective flows produce also a substantial (but downward) kinetic energy flux

$$\overline{F}_{\text{kin}} = \frac{1}{2} \overline{\rho \mathbf{u}^2 u_r}, \quad (26)$$

where  $\mathbf{u} = \mathbf{U} - \overline{\mathbf{U}}$ . Thus the total convected flux

$$\overline{F}_{\text{conv}} = \overline{F}_{\text{enth}} + \overline{F}_{\text{kin}}, \quad (27)$$

can be substantially different from the enthalpy flux. This is particularly true for the downflows, where the signs of the enthalpy and kinetic energy fluxes are opposite (cf. Figure 1 of

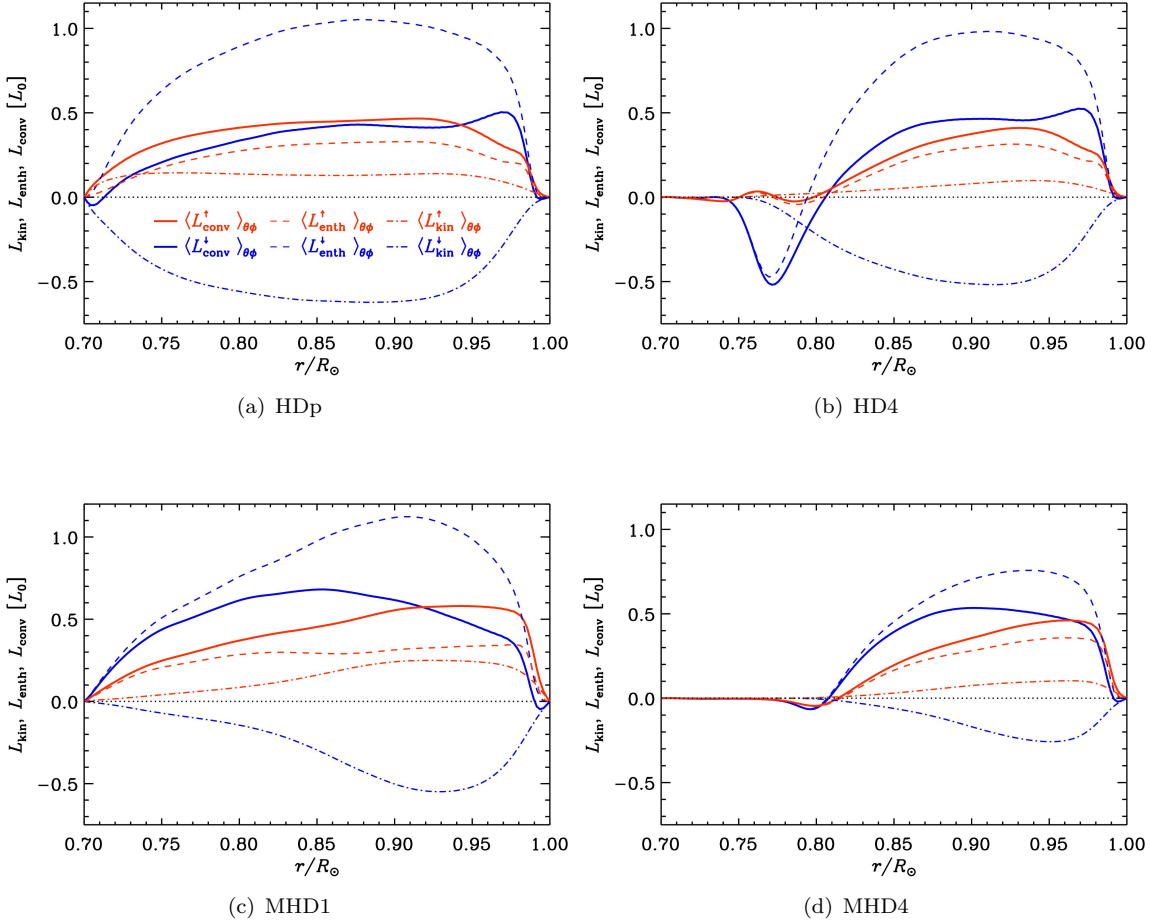


Figure 6. Convective (thick solid), enthalpy (dashed), and kinetic energy (dash-dotted) fluxes for upflows (red) and downflows (blue) from Runs HDp, HD4, MHD1, and MHD4 (colour online).

Käpylä *et al.* 2017b). An early study (Cattaneo *et al.* 1991) suggested that the two contributions nearly cancel for the downflows. However, later studies of Chan and Gigas (1992) and Brummell *et al.* (2002) confirmed that partial cancellation occurs, but that the downflows still contribute approximately equally much as the upflows to the total energy transport. The main difference between the study of Cattaneo *et al.* (1991) and those of Chan and Gigas (1992) and Brummell *et al.* (2002) is that the latter include a stably stratified overshoot layer below the CZ, whereas in the former the whole domain is convectively unstable.

We study the detailed flux dynamics by separating the convective flux into kinetic and enthalpy fluxes from up- and downflows and represent them in terms of the corresponding luminosities:

$$\langle L_{\text{conv}} \rangle_{\theta\phi} = \langle L_{\text{enth}} \rangle_{\theta\phi} + \langle L_{\text{kin}} \rangle_{\theta\phi}, \quad (28)$$

$$\langle L_{\text{enth}} \rangle_{\theta\phi} = \langle L_{\text{enth}}^{\uparrow} \rangle_{\theta\phi} + \langle L_{\text{enth}}^{\downarrow} \rangle_{\theta\phi}, \quad (29)$$

$$\langle L_{\text{kin}} \rangle_{\theta\phi} = \langle L_{\text{kin}}^{\uparrow} \rangle_{\theta\phi} + \langle L_{\text{kin}}^{\downarrow} \rangle_{\theta\phi}. \quad (30)$$

Here  $\uparrow$  and  $\downarrow$  refer to contributions from up- and downflows, respectively, and  $L_i = 4\pi r^2 F_i$  are the corresponding luminosities. Representative results are shown in figure 6 from Runs HDp, HD4, MHD1, and MHD4. We find that both  $\langle L_{\text{enth}}^{\downarrow} \rangle_{\theta\phi}$  and  $\langle L_{\text{kin}}^{\downarrow} \rangle_{\theta\phi}$  are large and of opposite sign, leading to a net positive  $\langle L_{\text{conv}}^{\downarrow} \rangle_{\theta\phi}$  that is much smaller than either of its constituents.

However,  $\langle L_{\text{conv}}^{\downarrow} \rangle_{\theta\phi}$  contributes equally, or more, than the upflows ( $\langle L_{\text{conv}}^{\uparrow} \rangle_{\theta\phi}$ ) to the total convected flux ( $\langle L_{\text{conv}} \rangle_{\theta\phi}$ ) in all cases. This agrees with the Cartesian simulations of [Chan and Gigas \(1992\)](#), [Brummell \*et al.\* \(2002\)](#) and [Käpylä \*et al.\* \(2017b\)](#). No qualitative difference is seen between setups without and with stably stratified overshoot and radiative layers. These results are contrasted with those of [Korre \*et al.\* \(2017\)](#) from Boussinesq convection, where the upflows contribute only to downward transport of thermal energy.

### 3.2. Force balance

Recently, [Käpylä \*et al.\* \(2017b\)](#) and [Hotta \(2017\)](#) studied the force balance on up- and downflows in non-rotating Cartesian convection. A remarkable result from these studies is that the downflows appear to feel the Schwarzschild criterion, such that they are accelerated in unstable and decelerated in stable regions, while the upflows do not appear to do so. Here we study whether this result holds also in astrophysically more realistic setups that include rotation and magnetic fields in spherical coordinates.

We study this by measuring the total force on the fluid

$$\mathcal{F}_r = \rho \frac{Du_r}{Dt}, \quad (31)$$

separately for the up- and downflows which are denoted by  $\uparrow$  and  $\downarrow$ , respectively. A positive (negative) force accelerates upflows (downflows). Representative results are shown in figure 7 for the same set of runs as in figure 6. Comparing the thick black-and-white and cyan curves in figure 7(a) and (e), it is seen that for Run HDp, the sign change of  $\mathcal{F}_r^{\downarrow}$  occurs roughly at the same average position as that of the radial entropy gradient (solid line black and white line). This appears to be the case also for  $\mathcal{F}_r^{\uparrow}$  at high latitudes and near the equator, whereas at mid-latitudes,  $\mathcal{F}_r^{\uparrow}$  is positive until roughly  $r \approx 0.85R_{\odot}$ . These results indicate that the downflows are accelerated in the Schwarzschild-unstable layer whereas the upflows accelerate mainly in the Schwarzschild-stable layer. This is clearly deviating from the behaviour of the Cartesian simulations with proper OZ and RZ, see [Käpylä \*et al.\* \(2017b\)](#) and [Hotta \(2017\)](#). However, as seen in figure 7(b) and (f) for Run HD4, the results of the Cartesian simulations are again restored: the downflows appear to adhere to the Schwarzschild criterion, while the upflows are accelerated in the stably stratified OZ, in the DZ, and in the lower part of the BZ.

The situation is significantly more complex in runs where rotation and magnetic fields are included. This is particularly clear in cases where the stably stratified layers are absent or very thin. This is seen, for example, in Run MHD1 in figure 7(c) and (g): at high latitudes, the upflows are accelerated everywhere except in a thin layer ( $r \gtrsim 0.95R_{\odot}$ ) near the surface, whereas the downflows are accelerated roughly above  $r \gtrsim 0.8R_{\odot}$ . The upflows are, however, driven upward also in the stably stratified OZ and DZ. No clear relation to the Schwarzschild criterion can be identified. At mid-latitudes around the tangent cylinder, the total force is downward for both, up- and downflows. Outside the tangent cylinder, the force is very roughly following a radially decreasing trend as a function of cylindrical radius. For runs with more substantial OZ, such as MHD4 in figure 7(d) and (h), the latitudinal variation is clearly weaker. The force on the upflows does not follow the Schwarzschild criterion in the deep parts in that the upflows are accelerated in the BZ as well as in the stably stratified DZ and OZ. The layer near the surface, where deceleration of the upflows occurs, is deeper near the equator also in these cases. The downflows, on the other hand, are decelerated in the lower part of the BZ well above the level where the Schwarzschild criterion indicates stability.

Although a detailed interpretation of the results is non-trivial, we can conclude that the presence of a substantial OZ has a significant influence on the large-scale dynamics of the

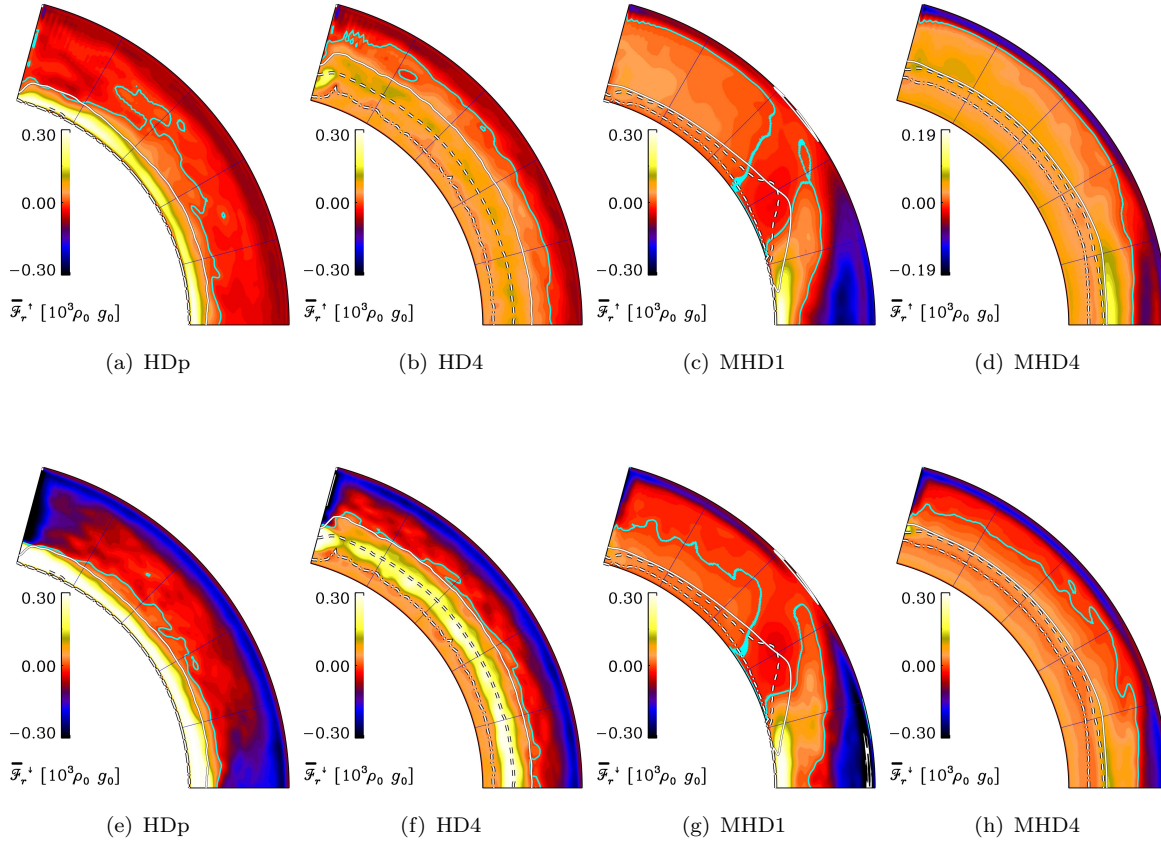


Figure 7. Total azimuthally averaged radial force  $\bar{\mathcal{F}}_r = \overline{\rho D u_r / Dt}$  on the upflows (upper row) and downflows (lower) for Runs HDp, HD4, MHD1, and MHD4. The thick cyan line indicates the zero level of the force. The black and white solid, dashed, and dash-dotted lines indicate the bottoms of the buoyancy, Deardorff, and overshoot zones, respectively (colour online).

system. Whether this is also the case in the Sun depends on the extent of overshooting at the base of the solar CZ. The recent results of [Hotta \(2017\)](#), who used Cartesian simulations to conclude that convective overshooting below the CZ of the Sun is only 0.4 per cent or 250 km, were used to argue that the interface between RZ and CZ could be well modelled by imposing suitable boundary conditions. However, these results are at odds with earlier models (e.g. [van Ballegoijen 1982](#), [Schmitt \*et al.\* 1984](#), [Pidatella and Stix 1986](#)) and helioseismic constraints (e.g. [Basu 2016](#)), which suggest an overshooting depth of the order of  $0.05\text{--}0.1H_p$  or 2500–5000 km. Furthermore, global rotation also changes the behaviour of the system qualitatively. The current study explores only a single rotation rate, leading to a rotationally constrained flow, at a modest supercriticality of convection. Studying the effects of rotation and higher Rayleigh numbers in more detail will be presented elsewhere.

### 3.3. Differential rotation

Some mean-field models of solar differential rotation ([Rempel 2005](#)) have invoked a subadiabatic lower part of the CZ to break the Taylor-Proudman constraint which, in turn, manifests itself through cylindrical isocontours of constant angular velocity. Given the subadiabatic layers in the current simulations, it is of interest to study the rotation profiles in comparison to earlier studies. We show in figure 8 the time-averaged rotation profiles from the MHD runs along with a hydrodynamic run, RHD2. The rotation rate is here chosen to be  $\Omega_0 = 3\Omega_\odot$  in

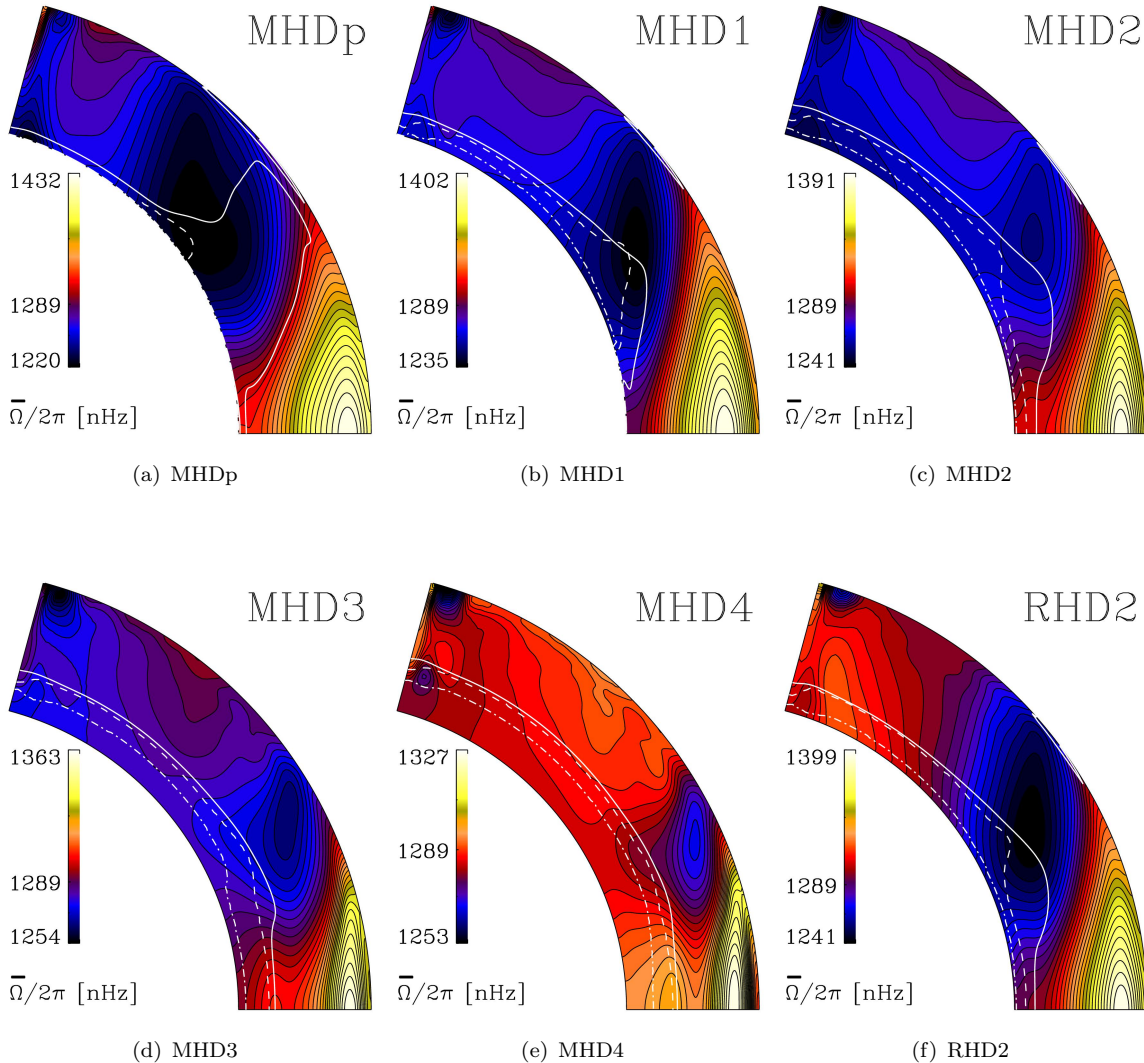


Figure 8. Time-averaged rotation profiles from the runs in the MHD set. The lower right panel shows Run RHD2 for comparison. The white solid, dashed, and dash-dotted lines indicate the bottoms of the BZ, DZ, and OZ, respectively (colour online).

order to reach a parameter regime where solar-like (fast equator, slow poles) differential rotation appears. Corresponding simulations with the solar rotation rate would lead to anti-solar differential rotation (e.g. Käpylä *et al.* 2014). Obtaining solar-like differential rotation with  $\Omega_0 = \Omega_\odot$  is challenging and can be achieved only if the radiative diffusion is unrealistically large (e.g. Fan and Fang 2014, Käpylä *et al.* 2014, Hotta *et al.* 2016) or the luminosity is artificially reduced (e.g. Hotta *et al.* 2015); see also the discussion in Appendix A of Käpylä *et al.* (2017a). Both approaches reduce the convective velocities and lead to a higher (lower) Coriolis (Rossby) number. To reach a solar-like regime,  $\text{Co} > 1$  ( $\text{Ro} < 1$ ) is needed (Käpylä *et al.* 2011a, Gastine *et al.* 2014, Brun *et al.* 2017, Viviani *et al.* 2018). The Coriolis numbers achieved in the present study ( $2.5 \lesssim \text{Co} \lesssim 4.6$ , see table 1) compare well with, for example, those of Nelson *et al.* (2013) who also used  $\Omega_0 = 3\Omega_\odot$  (see Appendix A of Käpylä *et al.* 2017a).

We find that the isocontours of  $\bar{\Omega} = \Omega_0 + \bar{U}_\phi/r \sin \theta$  are significantly tilted even in the run with a fixed heat conduction profile (MHDp). Furthermore, a mid-latitude minimum is visible, but it is shallower, and occupies a wider latitude range than in previous simulations with

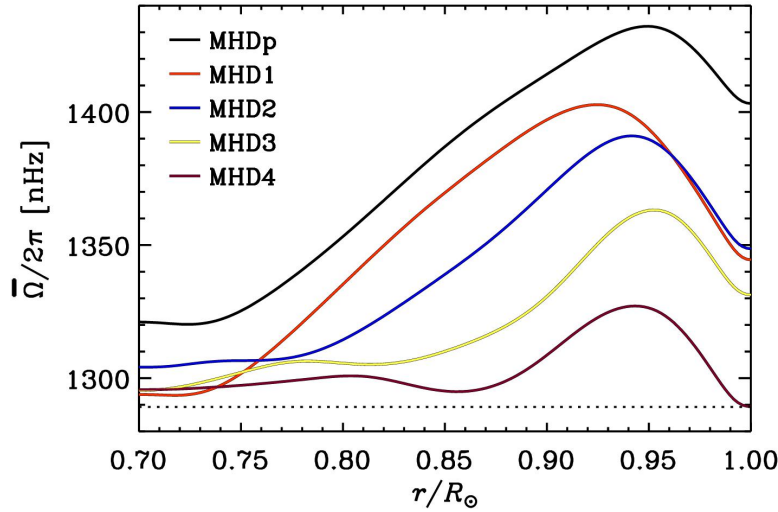


Figure 9. The mean angular velocity at the equator as a function of radius from the runs in the MHD set (colour online).

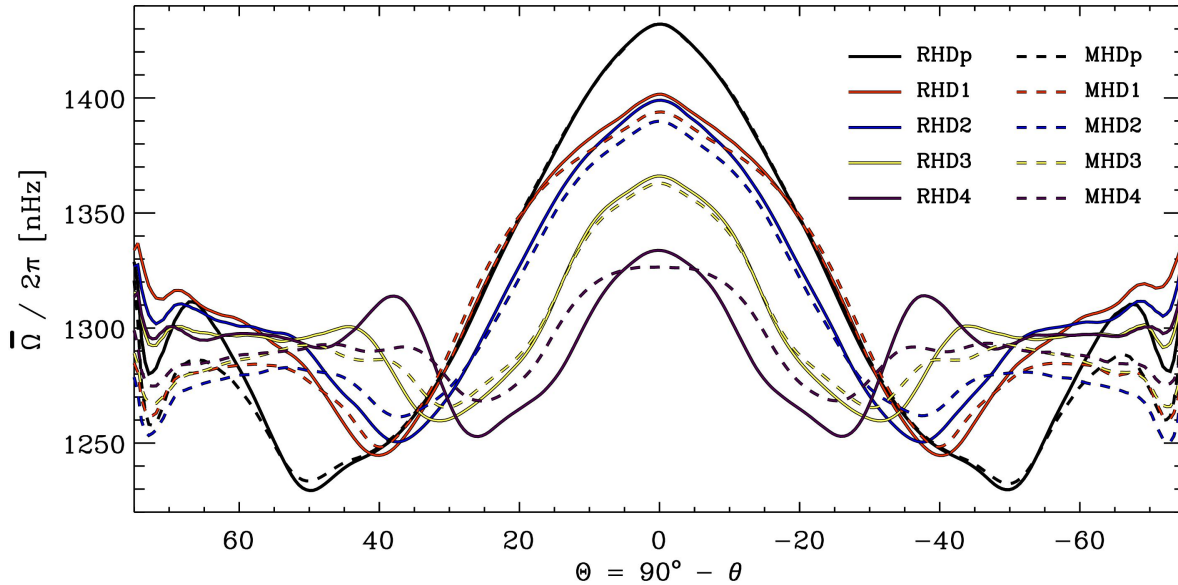


Figure 10. Mean angular velocity  $\bar{\Omega}$  from  $r = 0.95R_\odot$  from all runs in Sets RHD (solid lines) and MHD (dashed) (colour online).

similar rotation rates (see, e.g., Figure 4 of [Augustson et al. 2015](#) and Figure 1 of [Warnecke 2018](#)). The mid-latitude minimum is most likely responsible for the equatorward migrating activity seen in the aforementioned studies ([Warnecke et al. 2014](#)). A small NSSL, confined at low latitudes is also visible in the current runs; see figure 9. The most likely reason for its appearance is that the density stratification in the current runs is higher ( $\Delta\rho \approx 60$ ) than in earlier studies with otherwise similar parameters (e.g. [Käpylä et al. 2012](#), [Warnecke et al. 2014](#), [Käpylä et al. 2017a](#)) where  $\Delta\rho \approx 20$ . This has also been found in recent simulations of [Matilsky et al. \(2018\)](#). In theory, this allows the development of a NSSL, where the rotational influence on the flow is weak, quantified by  $\text{Co} < 1$  ([Rüdiger et al. 2014](#)). In such a parameter regime, the non-diffusive Reynolds stress, or  $\Lambda$  effect, responsible for the generation of differential rotation (e.g. [Rüdiger 1989](#)) reduces to a single term (e.g. [Käpylä 2018](#)) that drives a latitude-independent radial shear, as in [Barekat et al. \(2014\)](#) and [Kitchatinov \(2016\)](#). However, the current numerical results seem to confirm the results of [Robinson and Chan \(2001\)](#) in that

extreme density stratification (Hotta *et al.* 2015) is not required for the appearance of a NSSL. However, the detailed reproduction of, e.g., the solar NSSL does require high stratification and resolution to capture the small-scale surface convection and the shorter time scales near the surface.

In Runs MHD1 and MHD2, the rotation profile is qualitatively similar to that in MHDp. The clearest difference is the enhanced radial gradient of  $\bar{\Omega}$  near the surface at low latitudes. Also, the region of negative radial shear in mid-latitudes is enhanced—especially in the Deardorff layer in Run MHD2 (see the dashed and solid white lines in figure 8). In the remaining runs (MHD3 and MHD4), the layer of negative radial shear is even more pronounced, but appears predominantly within the BZ. It is also apparent that the differential rotation creeps into the radiative interior due to the relatively high diffusivities used in the current simulations. The local minimum of  $\bar{\Omega}$  at mid-latitudes, coinciding with the location of the tangent cylinder of the BZ to DZ transition near the equator, becomes more pronounced in Runs MHD3 and MHD4.

We show the rotation profile of a hydrodynamic run RHD2 in figure 8(f). The differences to the corresponding MHD run (MHD2) are most clearly visible at high latitudes, where the angular velocity is clearly reduced in the MHD run. Furthermore, the mid-latitude minimum of  $\bar{\Omega}$  is somewhat shallower in the MHD case. A similar trend is found in all runs in the RHD and MHD sets; see figure 10 for a comparison of  $\bar{\Omega}$  at  $r = 0.95R_{\odot}$ . The relatively weak influence of magnetic fields on differential rotation appears to differ from the results of Käpylä *et al.* (2017a), who found a strong quenching of mean flows in high resolution simulations. However, at comparable magnetic Reynolds numbers, as in the current simulations (roughly 30), the results of Käpylä *et al.* (2017a) also indicate only weak quenching; see their Figure 2 and Table 2.

The rotation profiles of Runs MHDp and MHD1 in particular clearly deviate from the Taylor-Proudman balance. To study this, we consider the mean vorticity equation:

$$\frac{\partial}{\partial t}(\nabla \times \bar{\mathbf{U}})_{\phi} = r \sin \theta \frac{\partial \bar{\Omega}^2}{\partial z} + (\nabla \bar{T} \times \nabla \bar{s})_{\phi} + \dots, \quad (32)$$

where  $\partial/\partial z = \cos \theta \partial/\partial r - r^{-1} \sin \theta \partial/\partial \theta$  is the derivative along the rotation axis, and the dots indicate terms due to Reynolds stress and molecular viscosity. We find that the first and second terms of the right-hand side, corresponding to the Coriolis force and the baroclinic effect, respectively, balance each other at all latitudes in Runs MHDp and MHD1; figures 11(a)–(b) and (d)–(e). The extended DZ of MHDp does not appear to lead to a significant enhancement of the baroclinic effect. In Run MHD4, the balance between Coriolis and baroclinic terms is realized only at low latitudes  $-30^{\circ} \gtrsim \theta \gtrsim 30^{\circ}$ . Furthermore, the magnitudes of both terms are clearly reduced in comparison to Runs MHDp and MHD1. This is likely to explain the more cylindrical isocontours of  $\bar{\Omega}$  in this run.

In a recent study, Käpylä *et al.* (2018a) showed that the large-scale properties of flows in hydrodynamic convection simulations, with the same model as here, are sensitive to changes in the thermal boundary conditions and the treatment of the unresolved photospheric layers. In particular, the setup used in the present study, with cooling near the surface and an isothermal top boundary condition, leads to larger deviations from the Taylor-Proudman balance than a corresponding setup where the energy in the near-surface layer is transported by SGS diffusion and where the upper boundary obeys a black body boundary condition. The latter was also used, for example, by Käpylä *et al.* (2017a). This suggests that the subadiabatic layer is not the main reason why the rotation profiles are more conical here than in previous studies.

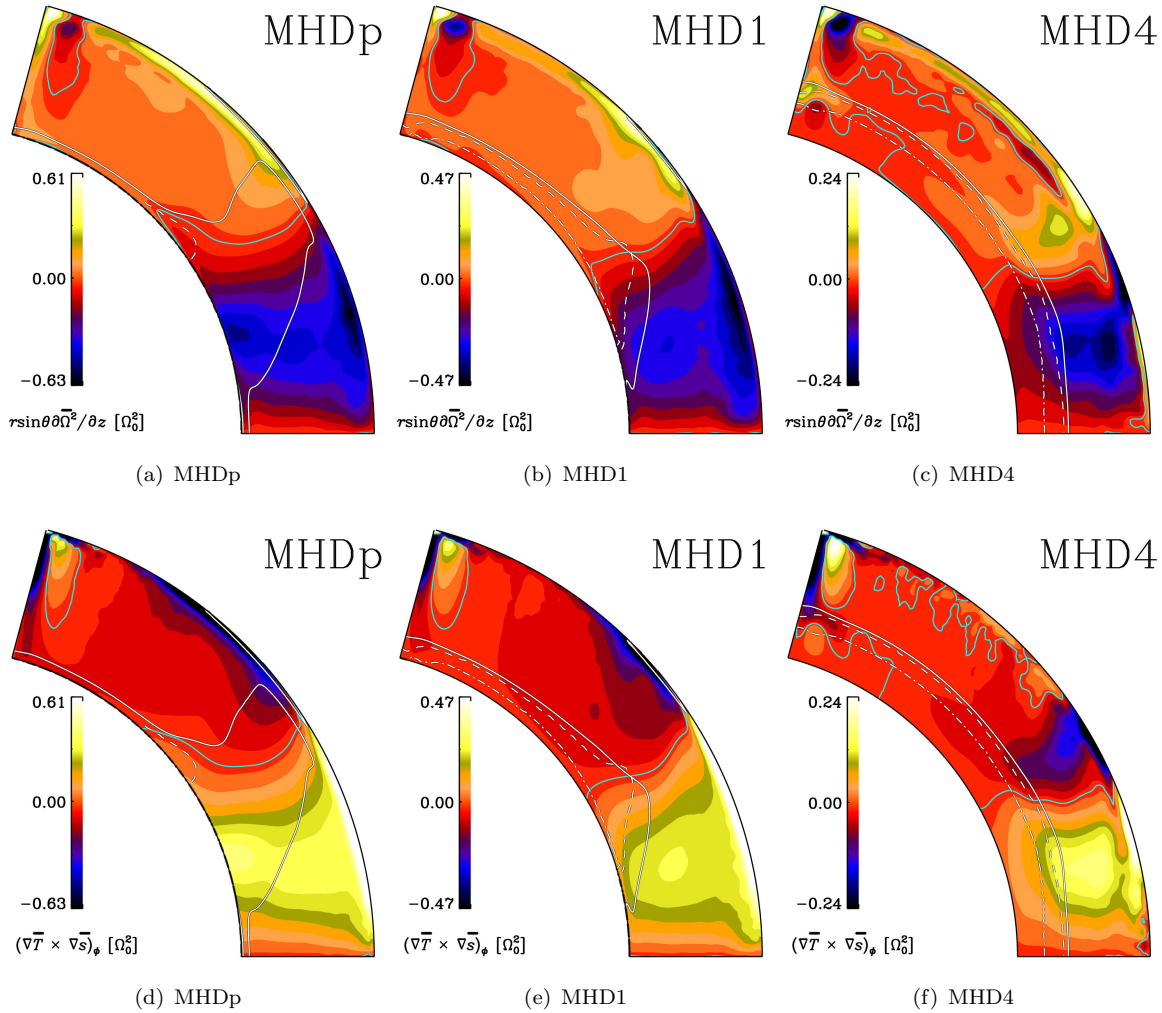


Figure 11. Dominant terms in the equation of mean azimuthal vorticity: Coriolis force  $r \sin \theta \partial \bar{\Omega}^2 / \partial z$  (upper row) and the baroclinic term  $(\nabla \bar{T} \times \nabla \bar{s})_\phi$  (lower row) in units of  $\Omega_0^2$  for Runs MHDp (left panel), MHD1 (middle), and MHD4 (right). The cyan line indicates the zero level whereas the white solid, dashed, and dash-dotted lines indicate the bottoms of the BZ, DZ, and OZ, respectively (colour online).

### 3.4. Horizontal velocity spectra

In recent studies, [Featherstone and Hindman \(2016a,b\)](#) investigated the effects of increasing supercriticality of convection and the rotational influence on the spectral energy distribution of convective flows in an effort to find clues to solve the convective conundrum. Furthermore, [Käpylä \*et al.\* \(2017b\)](#) found evidence that the structure of convective flows changes qualitatively when a smoothly varying heat conduction profile is used. Hence, next we study the effects of rotation, magnetic fields, and stably stratified layers on the spectral energy distribution in spherical domains. To calculate the power spectra for the horizontal velocity, we follow the same procedure as in [Featherstone and Hindman \(2016a\)](#). For each run, we consider a near-surface layer at  $r = 0.98R_\odot$  and calculate the normalised power spectrum:

$$P_\ell = \frac{\sum_{m=-\ell}^{\ell} |u_{\ell,m}|^2}{\sum_{\ell} \sum_{m=-\ell}^{\ell} |u_{\ell,m}|^2}. \quad (33)$$

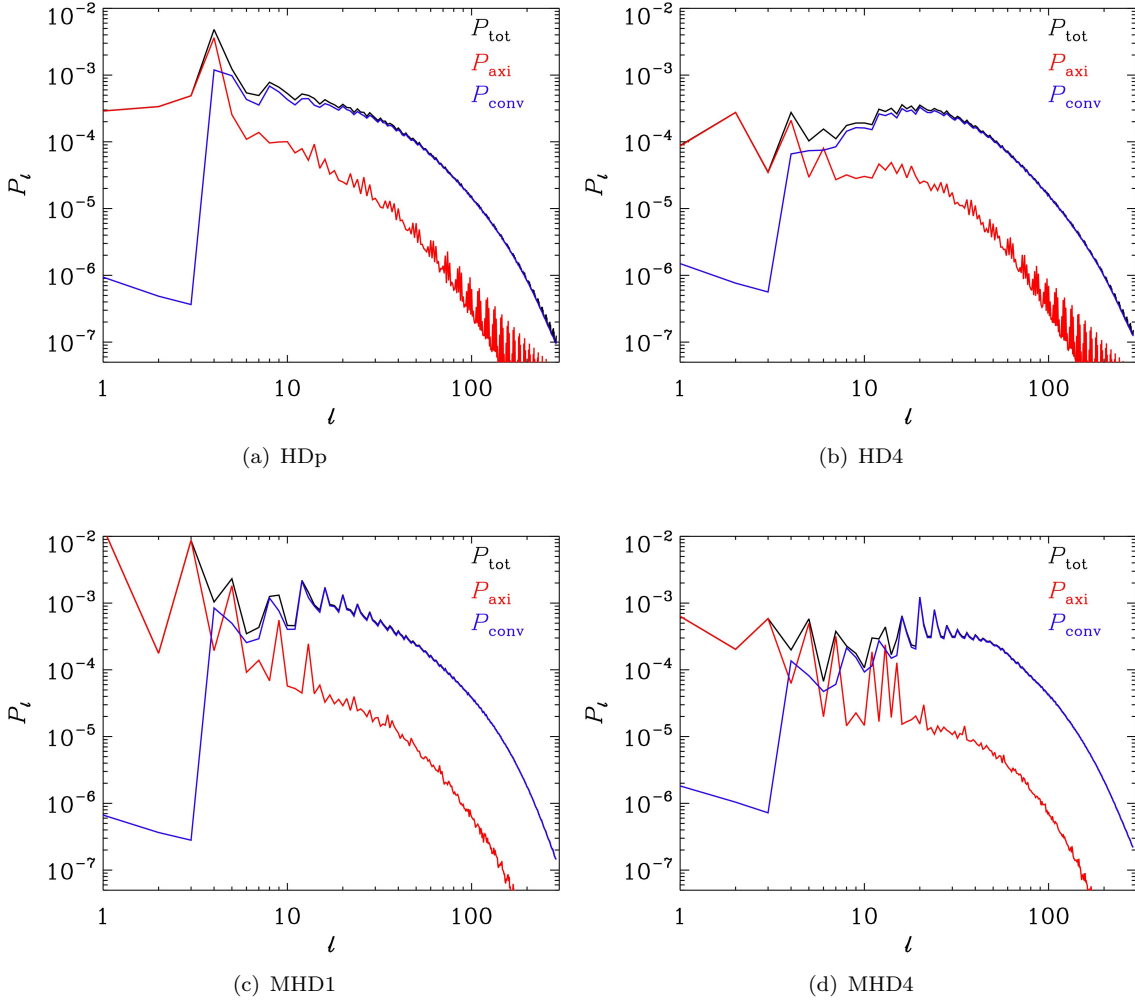


Figure 12. Power spectra of the total (black), axisymmetric (red), and non-axisymmetric (blue) parts of the velocity from runs (a) HDp, (b) HD1, (c) MHD1, and (d) MHD4 (colour online).

We separate the axisymmetric contribution,  $P_{\text{axi}}$ , given by the  $m = 0$  mode to obtain the convective velocity spectra,  $P_{\text{conv}}$ , as the sum of the higher  $m$  modes.

Figure 12 shows the results for four representative runs. Comparing panels (a) and (b), it is clear that a prescribed profile for the heat conductivity (Run HDp, panel a) leads to higher energy in the large scales than with Kramers profiles (Run HD4, panel b), when substantial OZ and RZ occur. The fact that the power at large scales is dominated by the axisymmetric component is due to a strong coherent meridional flow that develops in the system. Similar large-scale convective modes have been reported in non-rotating and slowly rotating simulations in the past (e.g. Brun and Palacios 2009, Käpylä *et al.* 2018b). In Run HD4, the meridional circulation becomes weaker, which explains the difference in the spectra. In addition, by increasing the radiative diffusivity in rotating MHD Runs MHD1 and MHD4, see figure 12(c) and (d), the total energy at large scales decreases by an order of magnitude and the peak in the convective spectra moves toward smaller scales, and the power at large scales in the axisymmetric velocity field becomes reduced. This is a consequence of weaker differential rotation; see figure 8. The reason for the changing distribution of the convective power is not so easily distinguishable. The rotational influence on the flow is changing by roughly 40 per cent between Runs MHD1 and MHD4 (see the sixth column of table 1) and it is unlikely that

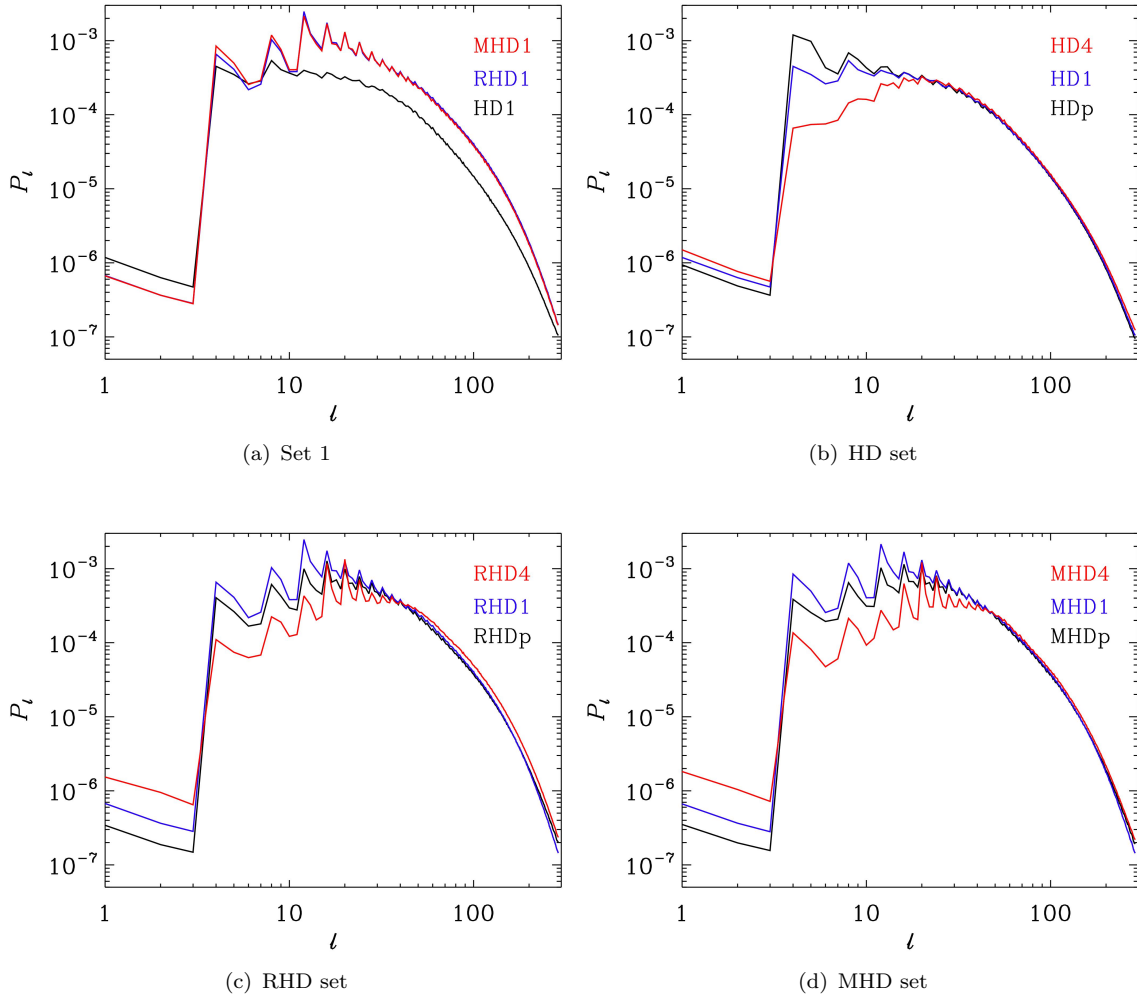


Figure 13. Comparison of the convective spectra  $P_{\text{conv}}$  from different runs: Runs HD1, RHD1, MHD1 with the same  $K_0$  (a), and for runs ‘p’, ‘1’, and ‘4’ in Sets HD (b), RHD (c), MHD (d), respectively (colour online).

this could have caused such a large effect. Another possibility is that some of the large-scale convective modes excited in Run MHD1 are absent in the shallower CZ of Run MHD4.

In figure 13 we compare the horizontal convective velocity spectra  $P_{\text{conv}}$  for different runs. In panel (a) we compare Kramers cases with the same value of  $K_0$ , but adding rotation and magnetic fields. Adding rotation has a marked effect in that the convective power is boosted at practically all scales. While a change from vertically to horizontally dominated turbulence as a function of rotation has been reported earlier from spherical convection simulations (e.g. Käpylä *et al.* 2014), the increase of the absolute magnitude of the horizontal flows is a new result. We find that these flows are enhanced especially in the upper parts of the CZ in the rotating runs. This could be because of shear-produced turbulence due to the strong differential rotation in these cases. Adding magnetic fields does not produce further visible difference. In the non-rotating Kramers runs, the energy at large scales decreases with increasing heat conductivity (panel (b)), while in the rotating cases in figures 13(c) and (d), the runs with lower heat conductivity have higher energy than the run with a prescribed profile. This is in accordance with figure 5. In the rotating cases, there seems to be a threshold: at low values of heat conductivity the energy at large scales is enhanced with respect to the same run with a prescribed profile, while increasing the value of  $K_0$  has the effect of decreasing the energy

at small values of  $\ell$ . This is also visible in figures 4(g), (h), and (i), where the luminosity is at first enhanced around the equator (Run MHD1), and then the transport of energy becomes almost isotropic throughout the CZ for Run MHD4. A possible explanation is that, while the depth of the convectively unstable layer diminishes, the horizontal extent of the largest excited convective modes is also reduced, thus lowering the power at the largest values of  $\ell$ . Allowing a self-consistent evolution of the heat conduction profile helps to reduce the energy at large scales, but does not affect the small scales. Moreover, the difference between a prescribed profile and Kramers runs is more marked in the non-rotating cases. Adding rotation reduces the effect of a Kramers-like opacity law.

In conclusion, we find that the effects of the Kramers-based heat conductivity on the velocity amplitudes are rather weak and they are not enough to resolve the problem of too high convective power in simulations in comparison to the Sun.

### 3.5. *Dynamo solutions*

We find that all of the current MHD simulations show large-scale dynamo action. Time-latitude diagrams of the mean azimuthal field are shown in figure 14. The solution in Run MHDp shows a cyclic large-scale field which, however, is relatively weak and stronger magnetic fields are mostly concentrated toward high latitudes. In Run MHD1, the solution does not show clear polarity reversals, although a quasi-periodic component clearly appears; see figure 14(b). This behaviour is qualitatively similar to that reported in Karak *et al.* (2015) and in Run E2 of Käpylä *et al.* (2017a), which, apart from the lower density stratification, has otherwise similar parameters as the current Run MHD1.

In Run MHD2, a clearly oscillatory mode is excited, which is reminiscent of earlier results (Käpylä *et al.* 2012, 2013, Augustson *et al.* 2015, Käpylä *et al.* 2016, Strugarek *et al.* 2017, Warnecke 2018). The main cycle period of a very similar run parameter-wise (Käpylä *et al.* 2016) was reported to be roughly 5 years, whereas here the cycle is shorter nearly by a factor of two. Representations of the magnetic fields in different phases of the cycle are shown in figure 15. Quantitative differences to Run MHD1 are relatively minor; the Reynolds and Coriolis numbers differ by roughly 15 per cent, see the fifth and sixth columns of table 1. However, the Deardorff layer is thicker at low latitudes and the region of negative radial shear is wider at mid-latitudes in Run MHD2 in comparison to Run MHD1. The dynamo solution thus appears to be sensitive to relatively small changes in the flow properties.

We also observe a quiescent period roughly between 15 and 25 years in physical time that can be interpreted as a Maunder minimum-type event (see also Augustson *et al.* 2015, Käpylä *et al.* 2016). During this event, also the dominant dynamo mode at the surface appears to change to a shorter one at late stages. The minimum event and the changing dynamo mode are due to a change of magnetic field structure in the deeper layers. This is illustrated in figure 14(f), where  $\bar{B}_\phi$  near the bottom of the CZ is shown. The period of the oscillatory mode at latitudes  $|\Theta| \gtrsim 30^\circ$  decreases after a readjustment around  $t = 15\text{--}25$  years. This is also where the polarity of the near-equator field changes, which could suggest a dynamo mode in the deep parts with a much longer period. The time series is too short to determine the dynamo period of its statistics reliably, however. These results are in agreement with the conclusions of Käpylä *et al.* (2016).

The total magnetic energy  $E_{\text{mag}}^{\text{tot}} = \langle \mathbf{B}^2/2\mu_0 \rangle_{\theta\phi}$  in Runs MHDp and MHD1 is on the order of  $10^4 \text{ J m}^{-3}$ ; see figure 16(a)–(b). The energy of the mean field  $E_{\text{mag}}^{\text{mean}} = \langle \bar{\mathbf{B}}^2/2\mu_0 \rangle_{\theta\phi}$ , on the other hand, is roughly 20–30 percent of  $E_{\text{mag}}^{\text{tot}}$  in MHDp and somewhat more in MHD1. The total kinetic energy  $E_{\text{kin}}^{\text{tot}} = \langle \rho \mathbf{U}^2/2 \rangle_{\theta\phi}$  is of the order of  $10^6 \text{ J m}^{-3}$  in MHDp and somewhat less in MHD1. The contribution of the mean flows (differential rotation and meridional circulation),  $E_{\text{kin}}^{\text{mean}} = \langle \rho \bar{\mathbf{U}}^2/2 \rangle_{\theta\phi}$ , is higher in MHDp in comparison to MHD1. This could reflect the effect

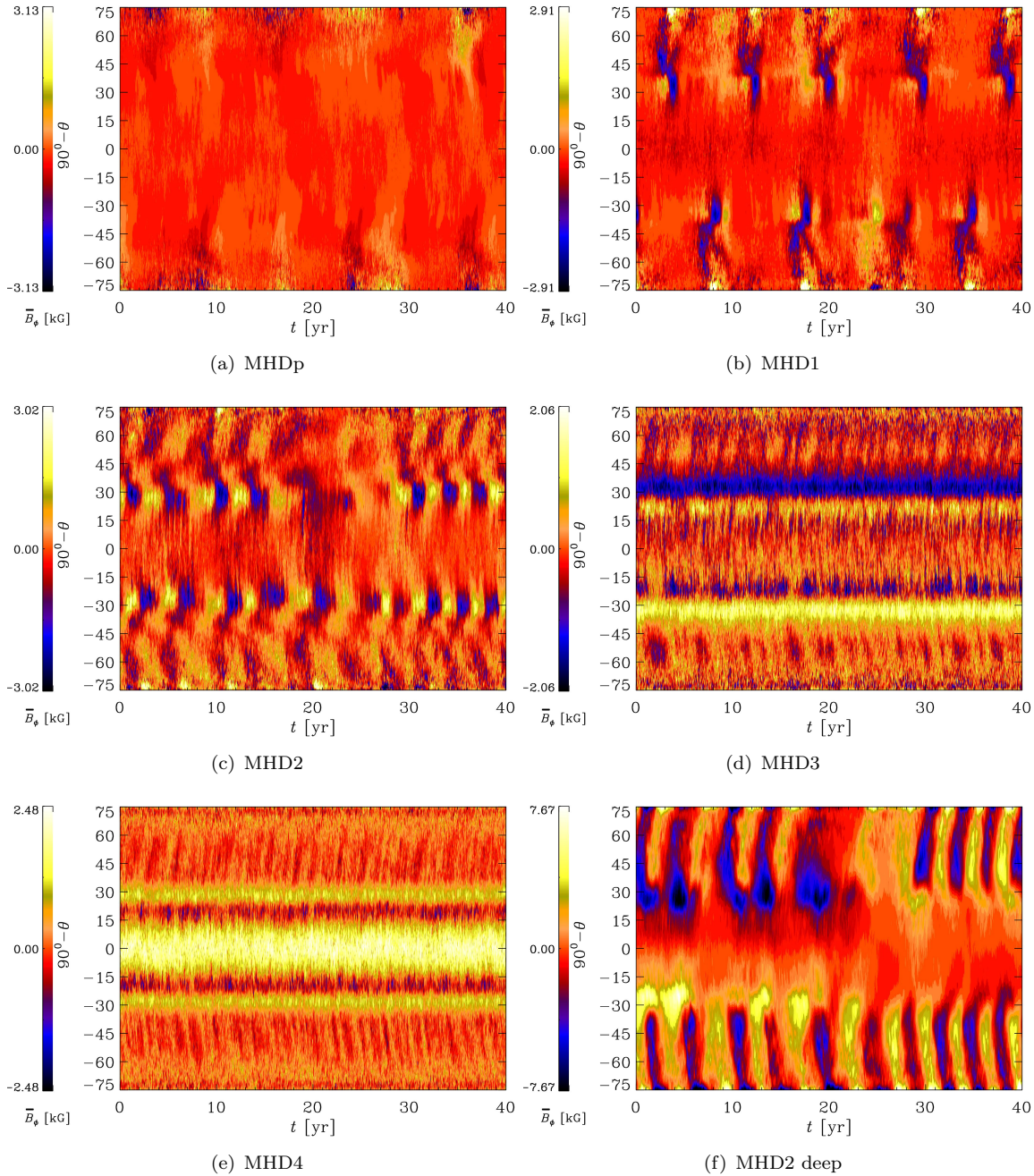


Figure 14. Panels (a)–(e): azimuthally averaged azimuthal magnetic field  $\bar{B}_\phi$  near the surface at  $r/R_\odot = 0.98$  as a function of time from a 40 year time span from the runs in the MHD set. Panel (f) shows the azimuthally averaged  $\bar{B}_\phi$  from  $r/R_\odot = 0.75$  from Run MHD2 from the same time span as in panel (c) (colour online).

of higher mean magnetic fields in the latter. The overall magnetic energy in these two runs is roughly an order of magnitude less than in runs with similar Coriolis number and Reynolds numbers in Käpylä *et al.* (2017a) (their run E2). The current runs differ from those of Käpylä *et al.* (2017a) in that the density stratification is roughly three times higher. Furthermore, the radial thermal boundary conditions and the treatment of the near-surface cooling differ from those used in Käpylä *et al.* (2017a) as explained in section 3.3. The dynamics of the simulations are sensitive to the thermal boundary conditions as well as the parameterisation

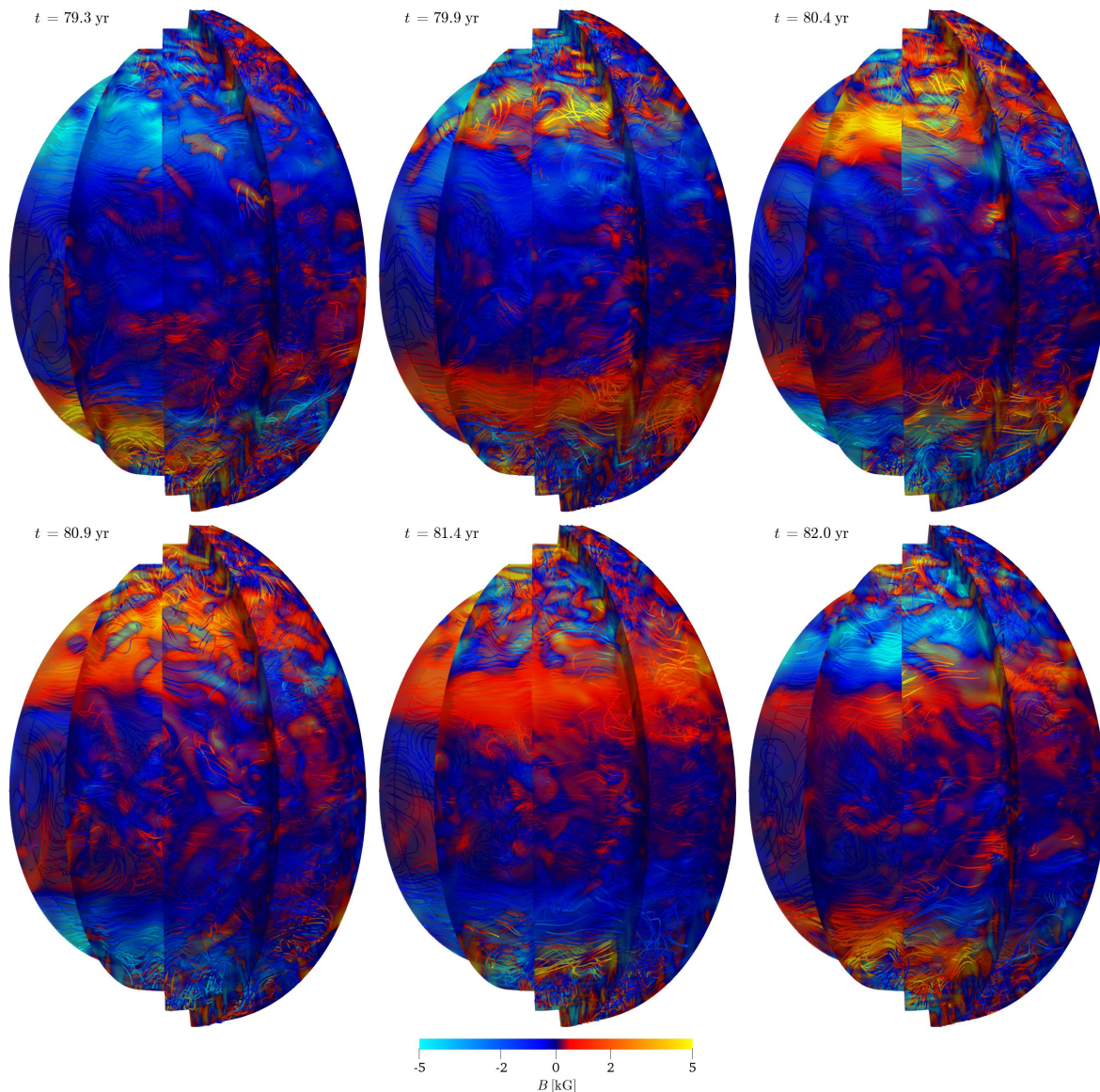


Figure 15. Magnetic fields lines and azimuthal magnetic field (colours) from six snapshots covering roughly one magnetic cycle from Run MHD2. The panels are separated by 0.5–0.6 years, as indicated by the legends. The colour bar indicates the field strength in kilogauss. An animated visualisation of the evolution of the magnetic field for this run is available in the online material (colour online).

of the near-surface layers (Käpylä *et al.* 2018a) which can also influence the dominant dynamo mode via the flow. Lastly, the SGS flux of entropy is here applied to the fluctuations as opposed to the total entropy. However, the current data is insufficient to track down the cause of the differences in the magnetic energy levels.

In Runs MHD3 and MHD4, the dynamo switches to a non-oscillatory mode. These solutions are superficially similar to quasi-stationary magnetic ‘wreaths’ at mid-latitudes found in several studies (e.g. Brown *et al.* 2010, Nelson *et al.* 2011). These runs did not, however, include a radiative layer below the convection zone, although they operate in a similar Coriolis number regime. One possible explanation is that the rotation profiles of these runs do not have a local minimum at mid-latitudes that is seen in later oscillatory solutions. In Runs MHD3 and MHD4, the surface appearance of the toroidal magnetic field reflects the occurrence of a large-scale field stored beneath the CZ in the stably stratified layers; see panel (c) of figure 16.

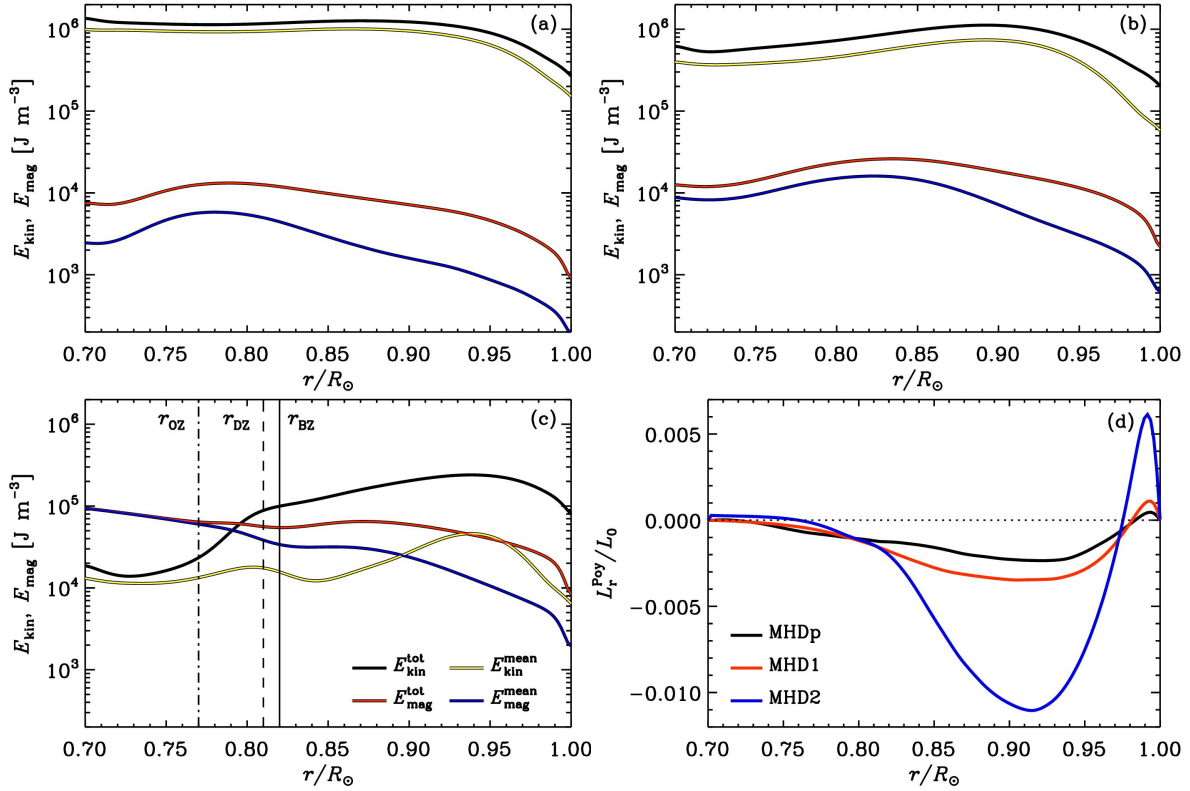


Figure 16. Horizontally and temporally averaged energy densities of the total flow (black), mean flow (yellow), total magnetic field (red), and mean magnetic field (blue) for Runs MHDp (a), MHD1 (b), and MHD4 (c). In panel (c) the bottoms of the BZ, DZ, and OZ are indicated with solid, dashed, and dash-dotted lines, respectively. Panel (d) shows the horizontally averaged luminosity corresponding to the radial Poynting flux for the same runs (colour online).

The overall magnitude of the magnetic field is significantly higher than in the cases without an RZ. We note that, for example, Guerrero *et al.* (2016), Warnecke (2018), and Strugarek *et al.* (2018) found changing dynamo modes as a function of the rotational influence on the flow. The Coriolis number based on the depth of the revised CZ varies by roughly 40 per cent in the runs of the MHD set; see the sixth column of table 1, which is a possible explanation for the change of the dominant dynamo mode.

We further study the magnetic energy transport due to the Poynting flux,

$$\mathbf{F}^{\text{Poy}} = (\mathbf{E} \times \mathbf{B})/\mu_0, \quad (34)$$

where  $\mathbf{E} = -\mathbf{U} \times \mathbf{B} + \eta\mu_0\mathbf{J}$  is the electric field. We consider the luminosity of the horizontally averaged radial component of  $\mathbf{F}^{\text{Poy}}$ ,  $\langle L_r^{\text{Poy}} \rangle_{\theta\phi} = 4\pi r^2 \langle F_r^{\text{Poy}} \rangle_{\theta\phi}$  in figure 16(d). The magnitude of  $\langle L_r^{\text{Poy}} \rangle_{\theta\phi}$  is at most on the order of one per cent of the total flux in Run MHD4 and between 0.2 and 0.3 per cent in Runs MHDp and MHD1. This suggests that the Poynting flux has an almost negligible effect on the total energy transport. Furthermore, the flux always points downwards, which agrees with previous results in Cartesian (Nordlund *et al.* 1992) and spherical (Brun *et al.* 2004) geometries.

Given that the dominant dynamo mode changes as a function of depth of the stably stratified layers below the CZ, it is of interest to study the diagnostics that are commonly held responsible for the generation of large-scale magnetic fields and cycles. One such diagnostic is the kinetic helicity of the flow, which can, for high conductivity, be associated with the  $\alpha$  effect of mean-field electrodynamics (Steenbeck *et al.* 1966, Krause and Rädler 1980). Furthermore, it has been shown by numerical simulations that the sign of the kinetic helicity can change under certain conditions in the deep parts of the convection zone and lead to a change

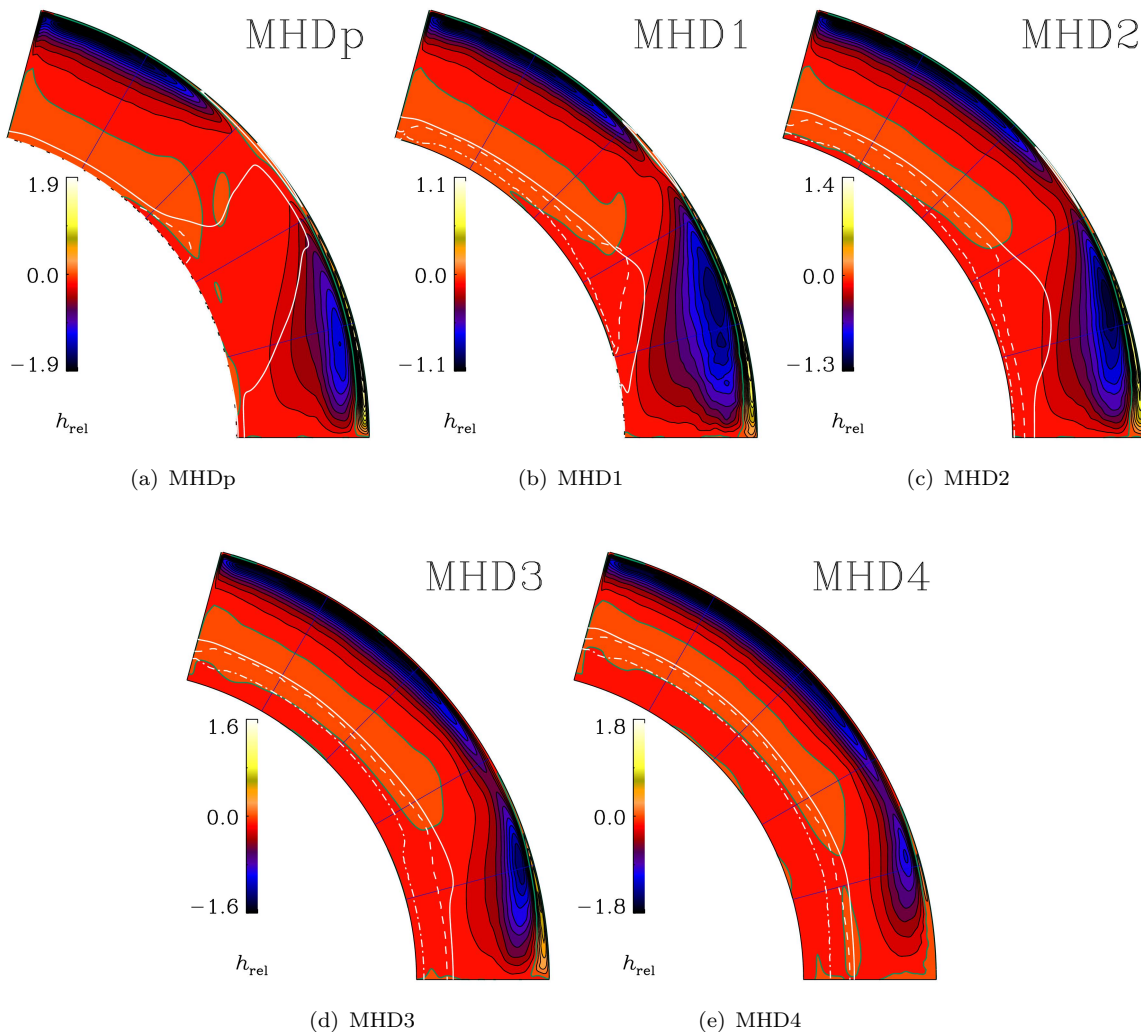


Figure 17. Time-averaged relative kinetic helicity from the MHD runs. As in figure 4, the black and white solid, dashed, and dash-dotted lines indicate the bottoms of the buoyancy, Deardorff, and overshoot zones, respectively. The green line indicates the zero level (colour online).

of the propagation direction of the dynamo wave (Duarte *et al.* 2016). Similar reversals have routinely been seen in simulations of stratified convection (Brandenburg *et al.* 1990, Käpylä *et al.* 2009), but the change in the migration direction occurs only for sufficiently deep helicity reversals, which is what was demonstrated by Duarte *et al.* (2016). Such reversals of the resulting  $\alpha$  effect have been utilised in mean-field dynamo theory starting with the work of Yoshimura (1972). The relevance of the kinetic helicity reversal for the Sun is that mean-field theory (Krause and Rädler 1980) and typical simulations (e.g. Ossendrijver *et al.* 2001, Käpylä *et al.* 2006) predict a positive  $\alpha$  effect in the northern hemisphere. Furthermore, a predominantly positive radial gradient of angular velocity is present in the solar CZ. In  $\alpha\Omega$  dynamos, this combination leads to poleward migration of dynamo waves due to the Parker–Yoshimura rule (Parker 1955, Yoshimura 1975). Thus, reversing the sign of  $\alpha$  would resolve this issue.

Figure 17 shows time-averaged relative kinetic helicity  $h_{\text{rel}} = \overline{\mathbf{u} \cdot \boldsymbol{\omega}} / u_{\text{rms}} \omega_{\text{rms}}$  from the MHD runs. Here,  $\boldsymbol{\omega} = \nabla \times \mathbf{u}$  is the vorticity of the fluctuating velocity. We do find a region of inverted helicity at the base of the CZ in all runs. However, this region is not very pronounced and is concentrated at high latitudes in Runs MHDp and MHD1–2. Although the region of positive helicity extends to lower latitudes in Runs MHD3 and MHD4, it is still confined within the

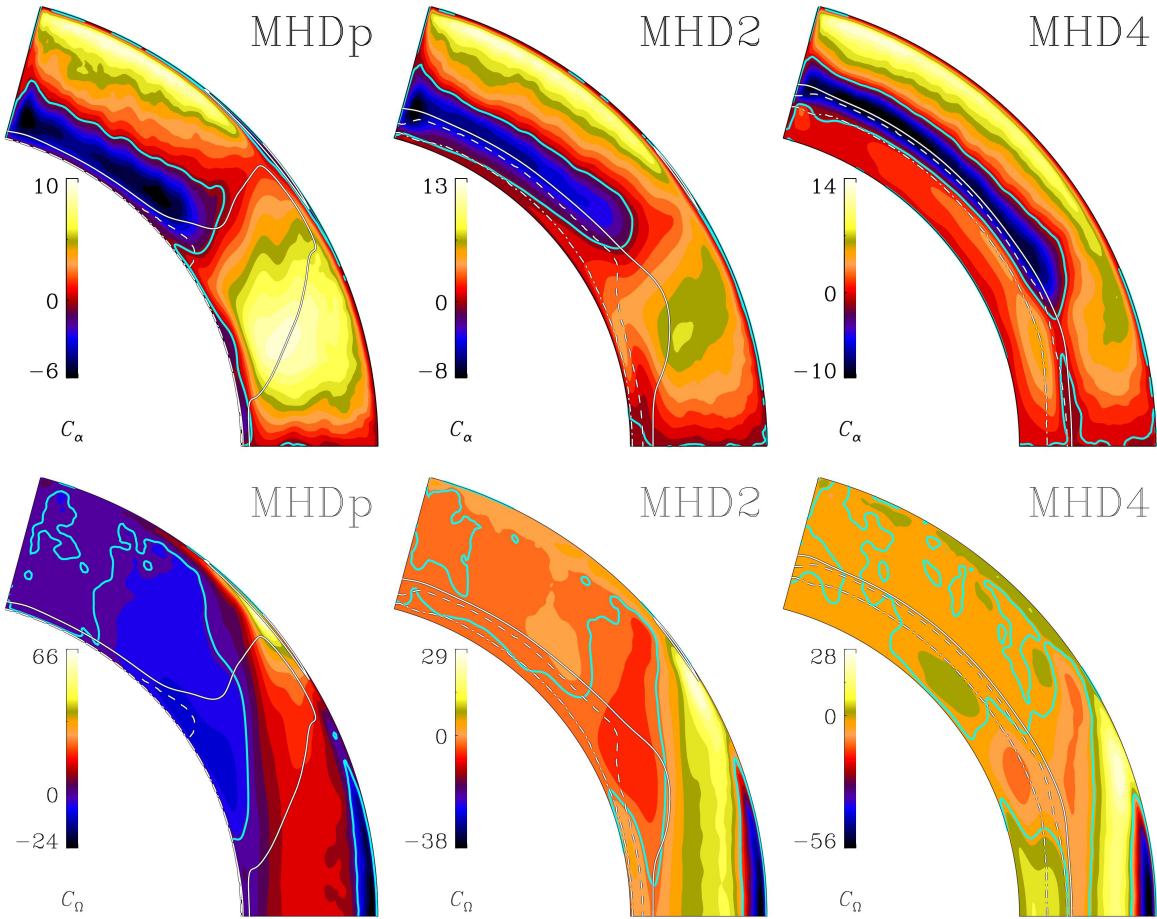


Figure 18. Dynamo numbers  $C_\alpha$  (upper row) and  $C_\Omega$  (lower row) for Runs MHDp (left panels), MHD2 (middle), and MHD4 (right). The cyan contours indicate the zero levels whereas the bottoms of the BZ, DZ, and OZ are indicated with solid, dashed, and dash-dotted lines, respectively (colour online).

tangent cylinder with respect to the bottom of the BZ. Only in Run MHD4, a clear inversion is seen at low latitudes near the equator.

The origin of the large-scale magnetic fields in the current simulations cannot be determined without a detailed analysis involving the computation of turbulent transport coefficients with, for example, the test-field method (e.g. Schinnerer *et al.* 2005, 2007, Warnecke *et al.* 2018). However, earlier studies (Warnecke *et al.* 2014, 2018) have indicated that, at least, the appearance of latitudinal dynamo waves can be fairly accurately predicted by the Parker–Yoshimura rule. This rule essentially states that the sign of the product of the  $\alpha$  effect and radial gradient of  $\Omega$  determines the propagation direction of the latitudinal dynamo wave. For an equatorward wave,  $\alpha \partial \bar{\Omega} / \partial r < 0$  in the northern hemisphere of the Sun. We proceed to study this by means of local dynamo numbers (as was also done in Käpylä *et al.* 2013)

$$C_\alpha = \frac{\alpha \Delta r}{\eta_{t0}}, \quad C_\Omega = \frac{\partial \bar{\Omega} / \partial r (\Delta r)^3}{\eta_{t0}}, \quad (35)$$

where  $\alpha = -\frac{1}{3} \tau (\overline{\mathbf{u} \cdot \boldsymbol{\omega}} - \overline{\mathbf{j} \cdot \mathbf{b}} / \bar{\rho})$  is a proxy of the  $\alpha$  effect, including the contributions from kinetic and current helicities (Pouquet *et al.* 1976). Furthermore,  $\eta_{t0} = \frac{1}{3} \tau u_{\text{rms}}^2(r, \theta)$  is an estimate of the turbulent magnetic diffusivity, where  $\tau = \alpha_{\text{MLT}} H_p / u_{\text{rms}}(r, \theta)$  is the convective turnover time,  $\alpha_{\text{MLT}} = 1.7$  is the mixing length parameter, and  $H_p = -(\partial \ln p / \partial r)^{-1}$  is the pressure scale height.

We show representative results of  $C_\alpha$  and  $C_\Omega$  in figure 18. In Run MHDp, the product  $C_\alpha C_\Omega$  is negative in the upper parts of the CZ at high latitudes and in a shallow layer near the equator. However, in the former (latter),  $C_\Omega$  ( $C_\alpha$ ) is small, which could explain the absence of cycles. In Run MHD2, a sizeable mid-latitude region shows a negative  $C_\alpha C_\Omega$ . This occurs at the same location where the equatorward migrating fields are seen in figure 14(c). A similar but somewhat smaller area appears also in Runs MHD3 and MHD4; see the rightmost panels of figure 18, although these runs do not support migrating solutions. A possible explanation is that the strong magnetic field developing in the radiative, strongly subadiabatic, layer forming in these runs is inhibiting dynamo migration. The behaviour seen in the current simulations with radiative layers is not likely to occur to the same extent in real stars where the small magnetic diffusivity will not allow substantial magnetic fields to penetrate into the radiative layers below the CZ.

#### 4. Conclusions

In the current study we have presented the first simulations of convection in rotating spherical coordinates with a heat conduction prescription based on the Kramers opacity law. In such models the radiative flux adapts to the thermodynamic state in a dynamical fashion such that the depth of the CZ is not fixed a priori. We have demonstrated that in such setups, the depth of the CZ is controlled by the overall efficiency of convective energy transport. Enhancing the radiative energy transport reduces the fraction of energy transported by convection in the deep parts, and is associated with the appearance of stably stratified Deardorff, overshoot, and radiative layers below the Schwarzschild-unstable layer. The enhanced luminosity in the current simulations implies a moderate Kelvin–Helmholtz time and allows the models to be evolved to a thermally saturated state in a reasonable time. Thus we do not have to resort to artificially enhancing the heat conductivity in the convectively stable layers immediately below the CZ (e.g. Brun *et al.* 2017, Hotta 2017). Such procedure leads to a more abrupt transition to the RZ and increased stiffness of the upper part of the CZ. This is likely to have repercussions for the interaction of the dynamics of the RZ and CZ. We have shown that the presence of such a stable layer has several interesting implications for the dynamics of convection.

Although the up- and downflows contribute roughly equally to the energy transport in all of the cases studied here, the presence of stably stratified overshoot and radiative layers are reflected in the force balance. This suggests fundamentally different dynamics in systems with and without such layers. In the rotating cases with  $\Omega_0 = 3\Omega_\odot$  and without significant stably stratified layers, the convective energy transport is highly anisotropic with mid-latitude regions producing an almost negligible contribution to the overall luminosity. If, on the other hand, stably stratified layers are present, the latitudinal dependence of convective energy transport is much weaker. Although the spectral power in convective motions is slightly reduced in cases with Kramers opacity, this effect is too small to account for the discrepancy between solar observations and simulations, most notably the problem of anti-solar differential rotation at solar parameters (e.g. Käpylä *et al.* 2014, Hotta *et al.* 2015).

The changes in the rotation profiles and large-scale magnetism are more subtle and the interpretation is less straightforward. However, the current simulations show clearly a NSSL at low latitudes—irrespective of the prescription of radiative diffusion. This is possibly due to the somewhat higher density stratification in the current simulations in comparison to several previous studies. The appearance of stably stratified layers at the bottom of the domain tends to produce a layer of negative radial shear at the base of the CZ. However, this leads to clearly equatorward migrating large-scale magnetic fields only in a single case. Although an inversion of the kinetic helicity is observed in the OZ and the lower parts of the CZ in our cases with

the shallowest convection zone, they exhibit quasi-stationary large-scale magnetic fields.

### Acknowledgement

The referees are acknowledged for their helpful comments on the manuscript. The authors wish to thank CSC – IT Center for Science Ltd. in Espoo, Finland, and the Gauss Center for Supercomputing through the Large-Scale computing project “Cracking the Convective Conundrum” in the Leibniz Supercomputing Centre’s SuperMUC supercomputer in Garching, Germany for computational resources. This work was supported in part by the Deutsche Forschungsgemeinschaft Heisenberg programme (grant No. KA 4825/1-1; PJK), the Academy of Finland ReSoLVE Centre of Excellence (grant No. 272157; MJK, PJK), the National Science Foundation Astronomy and Astrophysics Grants Program (grant 1615100), and the University of Colorado through its support of the George Ellery Hale visiting faculty appointment. MV acknowledges a postgraduate fellowship from the SOLSTAR Max Planck Research Group and the enrolment in the framework of the International Max Planck Research School for Solar System Science at the University of Göttingen (IMPRS) in Germany. FS was supported by the Max Planck Society grant “Science Projects in Preparation for the PLATO Mission.”

### References

- Augustson, K., Brun, A.S., Miesch, M. and Toomre, J., Grand minima and equatorward propagation in a cycling stellar convective dynamo. *Astrophys. J.*, 2015, **809**, 149.
- Barekat, A. and Brandenburg, A., Near-polytropic stellar simulations with a radiative surface. *Astron. Astrophys.*, 2014, **571**, A68.
- Barekat, A., Schou, J. and Gizon, L., The radial gradient of the near-surface shear layer of the Sun. *Astron. Astrophys.*, 2014, **570**, L12.
- Basu, S., Global seismology of the Sun. *Living Reviews in Solar Physics*, 2016, **13**, 2.
- Bekki, Y., Hotta, H. and Yokoyama, T., Convective velocity suppression via the enhancement of the subadiabatic layer: Role of the effective Prandtl number. *Astrophys. J.*, 2017, **851**, 74.
- Brandenburg, A., The case for a distributed solar dynamo shaped by near-surface shear. *Astrophys. J.*, 2005, **625**, 539–547.
- Brandenburg, A., Stellar mixing length theory with entropy rain. *Astrophys. J.*, 2016, **832**, 6.
- Brandenburg, A., Moss, D. and Tuominen, I., Stratification and thermodynamics in mean-field dynamos. *Astron. Astrophys.*, 1992, **265**, 328–344.
- Brandenburg, A., Nordlund, A. and Stein, R.F., Astrophysical convection and dynamos; in *Geophysical and Astrophysical Convection, Contributions from a workshop sponsored by the Geophysical Turbulence Program at the National Center for Atmospheric Research, October, 1995. Edited by Peter A. Fox and Robert M. Kerr. Published by Gordon and Breach Science Publishers, The Netherlands, 2000, p. 85-105*, edited by P.A. Fox and R.M. Kerr, Aug., 2000, pp. 85–105.
- Brandenburg, A., Tuominen, I., Nordlund, A., Pulkkinen, P. and Stein, R.F., 3-D simulation of turbulent cyclonic magneto-convection. *Astron. Astrophys.*, 1990, **232**, 277–291.
- Brown, B.P., Browning, M.K., Brun, A.S., Miesch, M.S. and Toomre, J., Persistent magnetic wreaths in a rapidly rotating Sun. *Astrophys. J.*, 2010, **711**, 424–438.
- Browning, M.K., Miesch, M.S., Brun, A.S. and Toomre, J., Dynamo action in the solar convection zone and tachocline: Pumping and organization of toroidal fields. *Astrophys. J. Lett.*, 2006, **648**, L157–L160.
- Brummell, N.H., Clune, T.L. and Toomre, J., Penetration and overshooting in turbulent compressible convection. *Astrophys. J.*, 2002, **570**, 825–854.
- Brun, A.S. and Browning, M.K., Magnetism, dynamo action and the solar-stellar connection. *Liv. Rev. Sol. Phys.*, 2017, **14**, 4.
- Brun, A.S., Miesch, M.S. and Toomre, J., Global-scale turbulent convection and magnetic dynamo action in the solar envelope. *Astrophys. J.*, 2004, **614**, 1073–1098.
- Brun, A.S. and Palacios, A., Numerical simulations of a rotating red giant star. I. Three-dimensional models of turbulent convection and associated mean flows. *Astrophys. J.*, 2009, **702**, 1078–1097.
- Brun, A.S., Strugarek, A., Varela, J., Matt, S.P., Augustson, K.C., Emeriau, C., DoCao, O.L., Brown, B. and Toomre, J., On differential rotation and overshooting in solar-like stars. *Astrophys. J.*, 2017, **836**, 192.
- Brun, A.S. and Toomre, J., Turbulent convection under the influence of rotation: Sustaining a strong differential rotation. *Astrophys. J.*, 2002, **570**, 865–885.
- Busse, F.H., Differential rotation in stellar convection zones. *Astrophys. J.*, 1970, **159**, 629.

- Cattaneo, F., Brummell, N.H., Toomre, J., Malagoli, A. and Hurlburt, N.E., Turbulent compressible convection. *Astrophys. J.*, 1991, **370**, 282–294.
- Chan, K.L. and Gigas, D., Downflows and entropy gradient reversal in deep convection. *Astrophys. J. Lett.*, 1992, **389**, L87–L90.
- Cossette, J.F. and Rast, M.P., Supergranulation as the Largest Buoyantly Driven Convective Scale of the Sun. *Astrophys. J. Lett.*, 2016, **829**, L17.
- Deardorff, J.W., The counter-gradient heat flux in the lower atmosphere and in the laboratory.. *J. Atmosph. Sci.*, 1966, **23**, 503–506.
- Deluca, E.E. and Gilman, P.A., Dynamo theory for the interface between the convection zone and the radiative interior of a star: Part I model equations and exact solutions. *Geophysical and Astrophysical Fluid Dynamics*, 1986, **37**, 85–127.
- Demarque, P., Guenther, D.B., Li, L.H., Mazumdar, A. and Straka, C.W., YREC: The Yale rotating stellar evolution code. Non-rotating version, seismology applications. *Astrophys. and Space Sci.*, 2008, **316**, 31–41.
- Dikpati, M. and Charbonneau, P., A Babcock-Leighton flux transport dynamo with solar-like differential rotation. *Astrophys. J.*, 1999, **518**, 508–520.
- Duarte, L.D.V., Wicht, J., Browning, M.K. and Gastine, T., Helicity inversion in spherical convection as a means for equatorward dynamo wave propagation. *Monthly Notices of the Roy. Astron. Soc.*, 2016, **456**, 1708–1722.
- Fan, Y. and Fang, F., A simulation of convective dynamo in the solar convective envelope: Maintenance of the solar-like differential rotation and emerging flux. *Astrophys. J.*, 2014, **789**, 35.
- Featherstone, N.A. and Hindman, B.W., The emergence of solar supergranulation as a natural consequence of rotationally constrained interior convection. *Astrophys. J. Lett.*, 2016a, **830**, L15.
- Featherstone, N.A. and Hindman, B.W., The spectral amplitude of stellar convection and its scaling in the high-Rayleigh-number regime. *Astrophys. J.*, 2016b, **818**, 32.
- Gastine, T., Yadav, R.K., Morin, J., Reiners, A. and Wicht, J., From solar-like to antisolar differential rotation in cool stars. *Monthly Notices of the Roy. Astron. Soc.*, 2014, **438**, L76–L80.
- Ghizaru, M., Charbonneau, P. and Smolarkiewicz, P.K., Magnetic cycles in global large-eddy simulations of solar convection. *Astrophys. J. Lett.*, 2010, **715**, L133–L137.
- Gilman, P.A., Nonlinear dynamics of Boussinesq convection in a deep rotating spherical shell. I.. *Geophys. Astrophys. Fluid Dynam.*, 1977, **8**, 93–135.
- Gilman, P.A. and Miller, J., Nonlinear convection of a compressible fluid in a rotating spherical shell. *Astrophys. J. Suppl.*, 1986, **61**, 585–608.
- Gizon, L. and Birch, A.C., Helioseismology challenges models of solar convection. *Proc. Nat. Acad. Sci.*, 2012, **109**, 11896–11897.
- Guerrero, G., Smolarkiewicz, P.K., de Gouveia Dal Pino, E.M., Kosovichev, A.G. and Mansour, N.N., On the role of tachoclines in solar and stellar dynamos. *Astrophys. J.*, 2016, **819**, 104.
- Hanasoge, S.M., Duvall, T.L. and Sreenivasan, K.R., Anomalously weak solar convection. *Proc. Natl. Acad. Sci.*, 2012, **109**, 11928–11932.
- Hotta, H., Solar overshoot region and small-scale dynamo with realistic energy flux. *Astrophys. J.*, 2017, **843**, 52.
- Hotta, H., Rempel, M. and Yokoyama, T., High-resolution calculation of the solar global convection with the reduced speed of sound technique. II. near surface shear layer with the rotation. *Astrophys. J.*, 2015, **798**, 51.
- Hotta, H., Rempel, M. and Yokoyama, T., Large-scale magnetic fields at high Reynolds numbers in magneto-hydrodynamic simulations. *Science*, 2016, **351**, 1427–1430.
- Hurlburt, N.E., Toomre, J. and Massager, J.M., Two-dimensional compressible convection extending over multiple scale heights. *Astrophys. J.*, 1984, **282**, 557–573.
- Käpylä, M.J., Käpylä, P.J., Olsper, N., Brandenburg, A., Warnecke, J., Karak, B.B. and Pelt, J., Multiple dynamo modes as a mechanism for long-term solar activity variations. *Astron. Astrophys.*, 2016, **589**, A56.
- Käpylä, P.J., Magnetic and rotational quenching of the  $\Lambda$  effect. *Astron. Astrophys.*(submitted), *arXiv:1712.08045*, 2018.
- Käpylä, P.J., Gent, F.A., Olsper, N., Käpylä, M.J. and Brandenburg, A., Sensitivity to luminosity, centrifugal force, and boundary conditions in spherical shell convection. *arXiv:1807.09309*, 2018a.
- Käpylä, P.J., Käpylä, M.J. and Brandenburg, A., Confirmation of bistable stellar differential rotation profiles. *Astron. Astrophys.*, 2014, **570**, A43.
- Käpylä, P.J., Käpylä, M.J. and Brandenburg, A., Small-scale dynamos in simulations of stratified turbulent convection. *Astron. Nachr.*, 2018b, **339**, 127–133.
- Käpylä, P.J., Käpylä, M.J., Olsper, N., Warnecke, J. and Brandenburg, A., Convection-driven spherical shell dynamos at varying Prandtl numbers. *Astron. Astrophys.*, 2017a, **599**, A4.
- Käpylä, P.J., Korpi, M.J. and Brandenburg, A., Alpha effect and turbulent diffusion from convection. *Astron. Astrophys.*, 2009, **500**, 633–646.
- Käpylä, P.J., Korpi, M.J., Brandenburg, A., Mitra, D. and Tavakol, R., Convective dynamos in spherical wedge geometry. *Astron. Nachr.*, 2010, **331**, 73.
- Käpylä, P.J., Korpi, M.J., Ossendrijver, M. and Stix, M., Magnetoconvection and dynamo coefficients. III.  $\alpha$ -effect and magnetic pumping in the rapid rotation regime. *Astron. Astrophys.*, 2006, **455**, 401–412.
- Käpylä, P.J., Mantere, M.J. and Brandenburg, A., Effects of stratification in spherical shell convection. *Astron.*

- Nachr.*, 2011a, **332**, 883.
- Käpylä, P.J., Mantere, M.J. and Brandenburg, A., Cyclic Magnetic Activity due to Turbulent Convection in Spherical Wedge Geometry. *Astrophys. J. Lett.*, 2012, **755**, L22.
- Käpylä, P.J., Mantere, M.J., Cole, E., Warnecke, J. and Brandenburg, A., Effects of enhanced stratification on equatorward dynamo wave propagation. *Astrophys. J.*, 2013, **778**, 41.
- Käpylä, P.J., Mantere, M.J., Guerrero, G., Brandenburg, A. and Chatterjee, P., Reynolds stress and heat flux in spherical shell convection. *Astron. Astrophys.*, 2011b, **531**, A162.
- Käpylä, P.J., Rheinhardt, M., Brandenburg, A., Arlt, R., Käpylä, M.J., Lagg, A., Olsper, N. and Warnecke, J., Extended subadiabatic layer in simulations of overshooting convection. *Astrophys. J. Lett.*, 2017b, **845**, L23.
- Karak, B.B., Käpylä, P.J., Käpylä, M.J., Brandenburg, A., Olsper, N. and Pelt, J., Magnetically controlled stellar differential rotation near the transition from solar to anti-solar profiles. *Astron. Astrophys.*, 2015, **576**, A26.
- Karak, B.B., Miesch, M. and Bekki, Y., Consequences of high effective Prandtl number on solar differential rotation and convective velocity. *Physics of Fluids*, 2018, **30**, 046602.
- Kitchatinov, L.L., Rotational shear near the solar surface as a probe for subphotospheric magnetic fields. *Astron. Lett.*, 2016, **42**, 339–345.
- Kitchatinov, L.L. and Rüdiger, G., Differential rotation in solar-type stars: Revisiting the Taylor-number puzzle. *Astron. Astrophys.*, 1995, **299**, 446.
- Korre, L., Brummell, N. and Garaud, P., Weakly non-Boussinesq convection in a gaseous spherical shell. *Phys. Rev. E*, 2017, **96**, 033104.
- Krause, F. and Rädler, K.H., *Mean-field Magnetohydrodynamics and Dynamo Theory*, 1980 (Oxford: Pergamon Press).
- Matilsky, L.I., Hindman, B.W. and Toomre, J., The Role of Downflows in Establishing Solar Near-Surface Shear. *arXiv:1810.00115*, 2018.
- Miesch, M.S., Brun, A.S. and Toomre, J., Solar differential rotation influenced by latitudinal entropy variations in the tachocline. *Astrophys. J.*, 2006, **641**, 618–625.
- Miesch, M.S. and Toomre, J., Turbulence, magnetism, and shear in stellar interiors. *Ann. Rev. Fluid Mech.*, 2009, **41**, 317–345.
- Mitra, D., Tavakol, R., Brandenburg, A. and Moss, D., Turbulent Dynamos in spherical shell segments of varying geometrical extent. *Astrophys. J.*, 2009, **697**, 923–933.
- Nelson, N.J., Brown, B.P., Brun, A.S., Miesch, M.S. and Toomre, J., Buoyant magnetic loops in a global dynamo simulation of a young Sun. *Astrophys. J. Lett.*, 2011, **739**, L38.
- Nelson, N.J., Brown, B.P., Brun, A.S., Miesch, M.S. and Toomre, J., Magnetic wreaths and cycles in convective dynamos. *Astrophys. J.*, 2013, **762**, 73.
- Nelson, N.J., Featherstone, N.A., Miesch, M.S. and Toomre, J., Driving solar giant cells through the self-organization of near-surface plumes. *Astrophys. J.*, 2018, **859**, 117.
- Nordlund, A., Brandenburg, A., Jennings, R.L., Rieutord, M., Ruokolainen, J., Stein, R.F. and Tuominen, I., Dynamo action in stratified convection with overshoot. *Astrophys. J.*, 1992, **392**, 647–652.
- O’Mara, B., Miesch, M.S., Featherstone, N.A. and Augustson, K.C., Velocity amplitudes in global convection simulations: The role of the Prandtl number and near-surface driving. *Adv. Space Res.*, 2016, **58**, 1475–1489.
- Ossendrijver, M., Stix, M. and Brandenburg, A., Magnetoconvection and dynamo coefficients: Dependence of the alpha effect on rotation and magnetic field. *Astron. Astrophys.*, 2001, **376**, 713–726.
- Parker, E.N., Hydromagnetic dynamo models. *Astrophys. J.*, 1955, **122**, 293.
- Parker, E.N., The dynamo dilemma. *Solar Phys.*, 1987, **110**, 11–21.
- Passos, D. and Charbonneau, P., Characteristics of magnetic solar-like cycles in a 3D MHD simulation of solar convection. *Astron. Astrophys.*, 2014, **568**, A113.
- Pidatella, R.M. and Stix, M., Convective overshoot at the base of the sun’s convection zone. *Astron. Astrophys.*, 1986, **157**, 338–340.
- Pouquet, A., Frisch, U. and Léorat, J., Strong MHD helical turbulence and the nonlinear dynamo effect. *J. Fluid Mech.*, 1976, **77**, 321–354.
- Pulkkinen, P., Tuominen, I., Brandenburg, A., Nordlund, A. and Stein, R.F., Rotational effects on convection simulated at different latitudes. *Astron. Astrophys.*, 1993, **267**, 265–274.
- Rempel, M., Solar differential rotation and meridional flow: The role of a subadiabatic tachocline for the Taylor-Proudman balance. *Astrophys. J.*, 2005, **622**, 1320–1332.
- Robinson, F.J. and Chan, K.L., A large-eddy simulation of turbulent compressible convection: Differential rotation in the solar convection zone. *Monthly Notices of the Roy. Astron. Soc.*, 2001, **321**, 723–732.
- Rüdiger, G., *Differential rotation and stellar convection. Sun and solar-type stars*, 1989 (Berlin: Akademie Verlag).
- Rüdiger, G., Egorov, P., Kitchatinov, L.L. and Küker, M., The eddy heat-flux in rotating turbulent convection. *Astron. Astrophys.*, 2005, **431**, 345–352.
- Rüdiger, G., Küker, M. and Tereshin, I., The existence of the  $\Lambda$  effect in the solar convection zone as indicated by SDO/HMI data. *Astron. Astrophys.*, 2014, **572**, L7.
- Schmitt, J.H.M.M., Rosner, R. and Bohn, H.U., The overshoot region at the bottom of the solar convection zone. *Astrophys. J.*, 1984, **282**, 316–329.
- Schou, J., Antia, H.M., Basu, S., Bogart, R.S., Bush, R.I., Chitre, S.M., Christensen-Dalsgaard, J., di Mauro,

- M.P., Dziembowski, W.A., Eff-Darwich, A., Gough, D.O., Haber, D.A., Hoeksema, J.T., Howe, R., Korzenik, S.G., Kosovichev, A.G., Larsen, R.M., Pijpers, F.P., Scherrer, P.H., Sekii, T., Tarbell, T.D., Title, A.M., Thompson, M.J. and Toomre, J., Helioseismic studies of differential rotation in the solar envelope by the solar oscillations investigation using the Michelson Doppler Imager. *Astrophys. J.*, 1998, **505**, 390–417.
- Schrinner, M., Rädler, K.H., Schmitt, D., Rheinhardt, M. and Christensen, U., Mean-field view on rotating magnetoconvection and a geodynamo model. *Astron. Nachr.*, 2005, **326**, 245–249.
- Schrinner, M., Rädler, K.H., Schmitt, D., Rheinhardt, M. and Christensen, U.R., Mean-field concept and direct numerical simulations of rotating magnetoconvection and the geodynamo. *Geophys. Astrophys. Fluid Dynam.*, 2007, **101**, 81–116.
- Spada, F., Demarque, P., Kim, Y.C., Boyajian, T.S. and Brewer, J.M., The Yale-Potsdam stellar isochrones. *Astrophys. J.*, 2017, **838**, 161.
- Spruit, H., Convection in stellar envelopes: A changing paradigm. *Mem. d. Soc. Astron. It.*, 1997, **68**, 397.
- Steenbeck, M., Krause, F. and Rädler, K.H., Berechnung der mittleren Lorentz-Feldstärke  $\mathbf{v} \times \mathbf{B}$  für ein elektrisch leitendes Medium in turbulenter, durch Coriolis-Kräfte beeinflusster Bewegung. *Zeitschrift Naturforschung Teil A*, 1966, **21**, 369.
- Strugarek, A., Beaudoin, P., Charbonneau, P. and Brun, A.S., On the sensitivity of magnetic cycles in global simulations of solar-like stars. *Astrophys. J.*, 2018, **863**, 35.
- Strugarek, A., Beaudoin, P., Charbonneau, P., Brun, A.S. and do Nascimento, J.D., Reconciling solar and stellar magnetic cycles with nonlinear dynamo simulations. *Science*, 2017, **357**, 185–187.
- Tremblay, P.E., Ludwig, H.G., Freytag, B., Fontaine, G., Steffen, M. and Brassard, P., Calibration of the mixing-length theory for convective white dwarf envelopes. *Astrophys. J.*, 2015, **799**, 142.
- van Ballegooijen, A.A., The overshoot layer at the base of the solar convective zone and the problem of magnetic flux storage. *Astron. Astrophys.*, 1982, **113**, 99–112.
- Vitense, E., Die Wasserstoffkonvektionszone der Sonne. *Z. Astrophys.*, 1953, **32**, 135.
- Viviani, M., Warnecke, J., Käpylä, M.J., Käpylä, P.J., Olsper, N., Cole-Kodikara, E.M., Lehtinen, J.J. and Brandenburg, A., Transition from axi- to nonaxisymmetric dynamo modes in spherical convection models of solar-like stars. *Astron. Astrophys.*, 2018, **616**, A160.
- Warnecke, J., Dynamo cycles in global convection simulations of solar-like stars. *Astron. Astrophys.*, 2018, **616**, A72.
- Warnecke, J., Käpylä, P.J., Käpylä, M.J. and Brandenburg, A., On the cause of solar-like equatorward migration in global convective dynamo simulations. *Astrophys. J. Lett.*, 2014, **796**, L12.
- Warnecke, J., Käpylä, P.J., Käpylä, M.J. and Brandenburg, A., Influence of a coronal envelope as a free boundary to global convective dynamo simulations. *Astron. Astrophys.*, 2016, **596**, A115.
- Warnecke, J., Rheinhardt, M., Tuomisto, S., Käpylä, P.J., Käpylä, M.J. and Brandenburg, A., Turbulent transport coefficients in spherical wedge dynamo simulations of solar-like stars. *Astron. Astrophys.*, 2018, **609**, A51.
- Weiss, A., Hillebrandt, W., Thomas, H.C. and Ritter, H., *Cox and Giuli's principles of stellar structure*, 2004 (Cambridge, UK: Cambridge Scientific Publishers Ltd).
- Yoshimura, H., On the dynamo action of the global convection in the solar convection zone. *Astrophys. J.*, 1972, **178**, 863–886.
- Yoshimura, H., Solar-cycle dynamo wave propagation. *Astrophys. J.*, 1975, **201**, 740–748.
- Zahn, J.P., Convective penetration in stellar interiors. *Astron. Astrophys.*, 1991, **252**, 179–188.